OPERATIONAL CHARACTERISTICS OF A ROTATING DETONATION ENGINE USING HYDROGEN AND AIR

THESIS

Rachel M Russo, Contractor, USAF

AFIT/GAE/ENY/11-J03

DEPARTMENT OF THE AIR FORCE
AIR UNIVERSITY

AIR FORCE INSTITUTE OF TECHNOLOGY

Wright-Patterson Air Force Base, Ohio

APPROVED FOR PUBLIC RELEASE; DISTRIBUTION UNLIMITED

The views expressed in this thesis are those of the author and do not reflect the official policy or position of the United States Air Force, Department of Defense, or the United States Government. This material is declared a work of the U.S. Government and is not subject to copyright protection in the United States.

AFIT/GAE/ENY/11-J03

OPERATIONAL CHARACTERISTICS OF A ROTATING DETONATION ENGINE USING HYDROGEN AND AIR

THESIS

Presented to the Faculty

Department of Aeronautics and Astronautics

Graduate School of Engineering and Management

Air Force Institute of Technology

Air University

Air Education and Training Command

In Partial Fulfillment of the Requirements for the

Degree of Master of Science in Aeronautical Engineering

Rachel M Russo, BS

Contractor, USAF

June 2011

APPROVED FOR PUBLIC RELEASE; DISTRIBUTION UNLIMITED

AFIT/GAE/ENY/11-J03

OPERATIONAL CHARACTERISTICS OF A ROTATING DETONATION ENGINE USING HYDROGEN AND AIR

Rachel M Russo, BS

Contractor, USAF

Approved:

_____	_____
Paul I. King (Chairman)	Date
_____	_____
Frederick R. Schauer (Member)	Date
_____	_____
Marcus D. Polanka (Member)	Date

AFIT/GAE/ENY/11-J03

Abstract

Rotating detonation engines (RDE) are pressure gain combustion engines that have the potential for greater efficiency than traditional, constant pressure, deflagration engines. RDEs are smaller and mechanically simpler than pulsed detonation engines. A small diameter (3 in) engine was successfully run on hydrogen and air. Most of the tests were conducted using air with a slightly lower diluents percentage (77% nitrogen as opposed to 79% nitrogen). These tests provided the foundation for determining the operational space (mass flow rate and equivalence ratio) of the rotating detonation engine. From the tests conducted with the lower diluents air, the appropriate run conditions for regular air were determined. For standard air (79% nitrogen) it was found that a larger equivalence ratio (about 1.5) was required to obtain continuous detonations.

Acknowledgements

I would like to thank Dr. Schauer for providing me with the opportunity to work in the Detonation Engine Research Facility. I truly enjoyed all the time I was able to spend in the lab and am grateful for such an opportunity.

I am grateful to Dr. King for the innumerable hours he spent discussing my results and providing suggestions for other ways to examine the data.

I also want to thank Curt Rice for all of his help throughout my research. He spent numerous hours answering my questions and fixing whatever was currently broken on the rig. Without his help, my research would not have gone as smoothly as it did.

I would also like to thank Andrew Naples and Capt Levi Thomas for sharing their knowledge of rotating detonation engines, the control program, and the specifics on the Pratt-Whitney engine.

Chris Stevens was willing to take the time to assist me in reducing the data I collected, answer any questions that I had, and help with high speed video collection. Without the time and effort he put in, I would not have been able to accomplish nearly as much as I did.

Finally, I would like to thank my husband for his continuous support and understanding throughout my time at AFIT.

TABLE OF CONTENTS

Page

Abstract iv

Acknowledgements v

List of Figures viii

List of Symbols xiii

I. Introduction 1
1.1 Efficiency for Detonation and Deflagration Engines 1
1.2 Previous Detonation Research 3
1.4 Chapter Preview 4

II. Literature Review 5
2.1 Pulsed Versus Continuous Detonation Engines 5
2.2 Previous Continuous Detonation Engine Research 7
2.2.1 Rotating Detonation Wave Structure. 7
2.4.2 Computational Fluid Dynamics Work. 8
2.4.3 Analytical Work 10
2.4.4 Previous Work on Hydrogen-Air Systems 11
2.4.5 Previous Air Force Research Laboratory Work 12

III. Facility and Test Setup 15
3.1 Detonation Engine Research Facility 15
3.2 Engine Setup 16
3.3 Air Supply 22
3.4 High Speed Video Footage 23
3.5 Successful Run Criteria 25
3.6 Data Collection 27
3.7 Data Reduction 28
3.8 Error Analysis 43

IV. Results and Discussion 46
4.1 Overview 46
4.2 Parameter Space, Enriched Air 46
4.3 Standard Air 49
4.3 Velocity, Enriched Air 53

V. Conclusions and Recommendations 57
5.1 Conclusions 57
5.2 Recommendations 59

Appendix A. One-Dimensional Detonation Wave Characteristics 60

Appendix B. Sensitivity Analysis Data 68

Appendix C. Time of Flight Code Velocity Graphs 70

Appendix D. Wave Front Direction Change 73

Appendix E. Uncertainty Tables 76

Appendix F. Full Test Space 85

References 88

LIST OF FIGURES

Page

Figure 1. Temperature-entropy and pressure-volume diagrams of Brayton and Humphrey cycles 3

Figure 2. First flight of PDE-driven aircraft 6

Figure 3. Annular cylinder combustion chamber 8

Figure 4. CFD model of rotating detonation wave structure (4) 9

Figure 5. Cold flow data for helium-air test (12) 13

Figure 6. Pratt-Whitney rotary detonation engine 16

Figure 7. Schematic of RDE 18

Figure 8. Instrumentation and propellant flow direction. 19

Figure 9. Propellant delivery system 20

Figure 10. Sample low-speed data acquired by LabView® 21

Figure 11. Cell width as a function of percent nitrogen 23

Figure 12. Mirror mount assembly 24

Figure 13. Pressure trace for a full-length run 26

Figure 14. Pressure trace for a run that did not stay in the channel 26

Figure 15. Time of flight code hold time 29

Figure 16. Zero standard deviations above the mean 31

Figure 17. One standard deviation above the mean 31

Figure 18. Two standard deviations above the mean 32

Figure 19. Final parameter comparison 33

Figure 20. Velocities for PCB 24 from time of flight code 34

Figure 21. Velocity graph of hydrogen-oxygen run (6) 35

Figure 22. Raw pressure data 36

Figure 23. Close up view of Fig. 22, counter-clockwise flow (PCB 26-25-24) 37

Figure 24. Close up view of Fig. 22, flow reversal (PCB 26-25-24 to PCB 24-25-26) .. 38

Figure 25. Close up view of Fig. 22, clockwise flow with varying velocities 38

Figure 26. Wave Front Flow Reversal, enriched air, total mass flow rate of 41.1 lbm/min 40

Figure 27. Close up view of Fig. 26 40

Figure 28. Wave front flow reversal, velocity graph, total mass flow rate of 41.1 lbm/min 41

Figure 29. Velocity from fast Fourier transform of pressure data 42

Figure 30. Histogram of velocity from time of flight code 42

Figure 31. Parameter space with linear lower boundary line 47

Figure 32. Parameter space for enriched air based on fuel mass flow rate 48

Figure 33. Parameter space for enriched air based on air and fuel mass flow rates 49

Figure 34. Equivalence ratio and fuel mass flow rate for successful enriched air and partially successful standard air runs 50

Figure 35. Equivalence ratio and total mass flow rate for enriched air and partially successful standard air runs 51

Figure 36. Parameter space for enriched air runs with successful standard air runs 53

Figure 37. Speed and equivalence ratio for total mass flow rates of 37-43 lbm/min 54

Figure 38. Speed and equivalence ratio for total mass flow rates of 43-49 lbm/min 55

Figure 39. Speed and equivalence ratio for total mass flow rates of 49-53 lbm/min 55

Figure 40. Speed and equivalence ratio for all successful enriched air runs 56

Figure 41. One-Dimensional model of a detonation wave 60

Figure 42. P-v Hugoniot curve with Rayleigh line 61

Figure 43. Rankine-Hugoniot curve 63

Figure 44. Rankine-Hugoniot curve with a Rayleigh line for higher wave speeds 65

Figure 45. Zeldovich, von Neumann, and Döring detonation wave profile 66

Figure 46. Wave speed data sample 1 φ=0.87, $\dot{m}_{tot}$=50.39 lbm/min, $\dot{m}_f$=1.4 lbm/min. 70

Figure 47. Wave speed data sample 2 φ=1.13, $\dot{m}_{tot}$=51.72 lbm/min, $\dot{m}_f$=1.8 lbm/min. 70

Figure 48. Wave speed data sample 3 φ=1.6, $\dot{m}_{tot}$=41.1 lbm/min, $\dot{m}_f$=2 lbm/min..... 71

Figure 49. Wave speed data sample 4 φ=1.18, $\dot{m}_{tot}$=24.4 lbm/min, $\dot{m}_f$=0.8 lbm/min... 71

Figure 50. Wave front direction change, enriched air, total mass flow rate of 51.7 lbm/min 73

Figure 51. Close up view of Fig. 50..... 73

Figure 52. Wave front flow reversal, velocity graph, enriched air, total mass flow rate of 51.7 lbm/min 74

Figure 53. Wave front direction change for standard air, non-repeatable run, total mass flow rate of 23.8 lbm/min 74

Figure 54. Close up view of Fig. 53..... 75

Figure 55. Wave front flow reversal, velocity graph, standard air, non-repeatable run, total mass flow rate of 23.8 lbm/min 75

Figure 56. Full test space 85

Figure 57. Standard air full test space, partially successful runs delineated by channel width 86

LIST OF TABLES

Page

Table 1. Propellant feed pressures 17

Table 2. Standard air run conditions and results 52

Table A 1. Hugoniot curve region classifications 64

Table B 1. Case 1 sensitivity analysis data 68

Table B 2. Case 2 sensitivity analysis data 69

Table E 1. Equivalence ratio, total mass flow rate and detonation velocity errors for repeatable enriched air runs 76

Table E 2. Air and fuel mass flow rate errors for repeatable enriched air runs 77

Table E 3. Detonation and non-detonation velocity comparison for repeatable enriched air runs 78

Table E 4. Equivalence ratio, total mass flow rate and detonation velocity errors for non-repeatable enriched air runs 79

Table E 5. Air and fuel mass flow rate errors for non-repeatable enriched air runs 79

Table E 6. Detonation and non-detonation velocity comparison for non-repeatable enriched air runs 79

Table E 7. Equivalence ratio, total mass flow rate and detonation velocity errors for 2mm channel standard air runs 80

Table E 8. Air and fuel mass flow rate errors for 2mm channel standard air runs 80

Table E 9. Detonation and non-detonation velocity comparison for 2mm channel standard air runs 80

Table E 10. Equivalence ratio, total mass flow rate and detonation velocity errors for

6mm channel standard air runs 81

Table E 11. Air and fuel mass flow rate errors for 6mm channel standard air runs 81

Table E 12. Detonation and non-detonation velocity comparison for 6mm channel standard air runs 81

Table E 13. Equivalence ratio, total mass flow rate and detonation velocity errors for 10mm channel standard air runs 82

Table E 14. Air and fuel mass flow rate errors for 10mm channel standard air runs 83

Table E 15. Detonation and non-detonation velocity comparison for 10mm channel standard air runs 84

LIST OF SYMBOLS

Acronyms

AFRL	Air Force Research Laboratory
CFD	Computational fluid dynamics
CJ	Chapman-Jouguet
DERF	Detonation Engine Research Facility
FFT	Fast Fourier Transform
NRL	Naval Research Laboratory
PDE	Pulsed detonation engine
RDE	Rotating detonation engine
TDW	Transverse detonation wave

Symbols	[SI units] {English units}
B_x	bias error
c	speed of sound [m/s] {ft/s}
C_p	constant pressure specific heat [J/(kg*K)] {BTU/(lbm*R)}
C_v	constant volume specific heat [J/(kg*K)] {BTU/(lbm*R)}
d	diameter [m] {ft}
h	specific enthalpy [J/g] {BTU/lbm}
$h_f°$	enthalpy of formation [J/mol] {BTU/mol}
h*	critical propellant height [m] {ft}
m_dot	mass flow rate [g/s] {lbm/s}
M	Mach number
n	total number of variables
N	total number of data points in a sample
P	pressure [atm] {psi}
P_x	precision error
q	heat release [J/g] {BTU/lbm}
R	universal gas constant [J/(mol*K)] {(ft^3*psi*lbm)/(mol*R)}
s	entropy [J/K] {BTU/R}
S_x	sample standard deviation
T	temperature [K] {R}
u	velocity [m/s] {ft/s}
v	specific volume [m^3/g] {ft^3/lbm}
V	volume [m^3] {ft^3}
x	number of consecutive points above threshold
X_bar	sample mean
Y	mass fraction

Greek Symbols	[SI units] {English units}
γ	specific heat ratio
Δ	channel width [m] {ft}
η	thermal efficiency
λ	detonation cell size [mm] {in}

Greek Symbols (continued)

ρ	density [g/m^3] {lbm/ft^3}
φ	equivalence ratio

Subscripts

b	back
B	Brayton
c	chamber
D	detonation
f	fuel
H	Humphrey
i	individual
j	individual
min	minimum
ref	reference
tot	total

OPERATIONAL CHARACTERISTICS OF A ROTATING DETONATION ENGINE USING HYDROGYN AND AIR

I. INTRODUCTION

Recently the Air Force has been exploring options for both reducing spending and conserving resources. One of the focus areas has been the use of jet fuel. A potential way to decrease the amount of jet fuel used is the creation of a more efficient engine. Therefore, a recent interest in propulsion research has been detonation engines as they have the potential to be more efficient than standard deflagration engines.

A deflagration reaction is characterized by a low flame speed and relatively constant pressure. In contrast, a detonation combustion process is characterized by a high flame speed coupled to a shock wave moving at a supersonic velocity, with a rise in pressure and density behind the detonation. Detonations are typically considered an approximately constant volume or pressure rise process.

1.1 Efficiency for Detonation and Deflagration Engines

The classification of a combustion process as a constant pressure or constant volume process affects the way thermal efficiency is calculated. For traditional engines, thermal efficiency (η_B) is calculated from an ideal Brayton cycle, which is based upon

the ratio of the temperatures before (T_0) and after (T_1) the isentropic expansion (Eq. 1) (1).

$$\eta_B = 1 - \frac{T_0}{T_1} \tag{1}$$

Detonation engines, however, are modeled as Humphrey cycles (1) in order to account for the approximately constant volume, pressure increase during the cycle (Fig. 1). Since the Humphrey cycle accounts for the ratio of the temperatures before (T_1) and after (T_2) combustion as well as the ratio of temperatures before (T_0) and after (T_1) the isentropic expansion, the efficiency (η_H) of a detonation combustion tends to be higher than that for a deflagration (1).

$$\eta_H = 1 - \frac{T_0}{T_1}\gamma\left[\frac{\left(\frac{T_2}{T_1}\right)^{1/\gamma} - 1}{\frac{T_2}{T_1} - 1}\right] \tag{2}$$

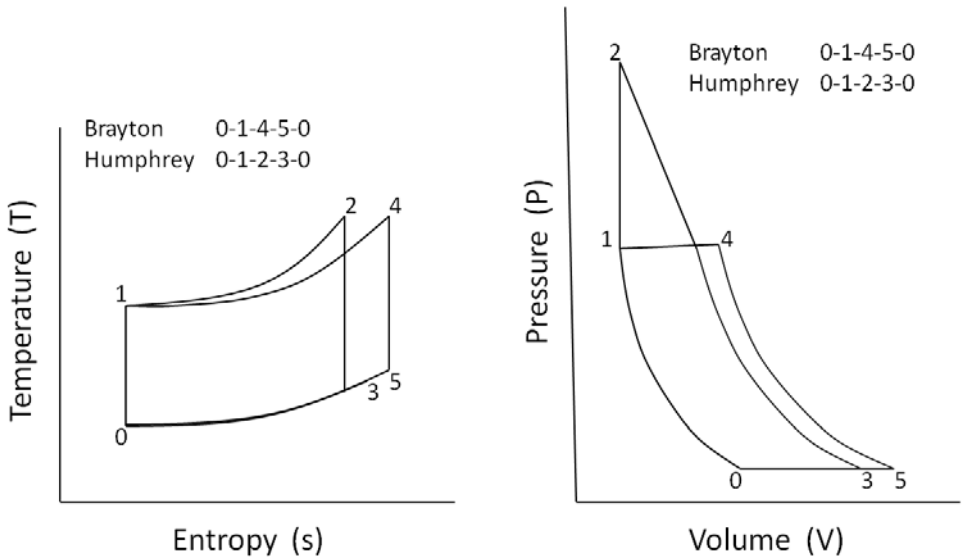

Figure 1. Temperature-entropy and pressure-volume diagrams of Brayton and Humphrey cycles

1.2 Previous Detonation Research

In the past, the focus of detonation research has primarily been on pulsed detonation engines (PDEs). Recently, however, detonation research has begun to also focus on rotating, or continuous, detonation engines (RDEs). Since RDEs do not need long exhaust tubes, RDEs can be shorter than equivalent PDEs. Also, RDEs could work more efficiently with a turbine since the exhaust from the RDE would provide the turbine a continuous stream instead of a series of pulses.

Previous research on RDEs has focused on characterizing the structure of the detonation wave front, appropriate methods to size the combustor, and cycle characterization. Beginning in the late 1950s, Russian scientists (2) characterized the detonation waves in gases as spinning while propagating down the length of a detonation tube. This wave structure closely resembles the transverse detonation wave seen in the

annulus of a RDE in later studies (3). Researchers at the Naval Research Laboratory (NRL) (4) have generated two and three dimensional numerical models of a continuous detonation combustor in order to examine the flow field and the effects of both back pressure and inlet stagnation pressure on the flow field (discussed in Chapter 2).

Historically there have been three primary difficulties associated with RDE research. These difficulties include running an RDE on hydrogen-air, initiating steady detonation propagation, and overcoming the pressure losses across the inlet.

1.3 Current Research Objectives

The objective of the current research is to determine the ranges of total mass flow rate and equivalence ratios in which a RDE will operate. The test setup used is comprised of a combustion chamber situated in a rig on loan from a Pratt and Whitney continuous detonation engine and is run with hydrogen and air as propellants.

1.4 Chapter Preview

Chapter 2 contains a discussion on detonation engines, both pulsed and continuous, and includes previous experimental, numerical and analytical work done on RDEs. Chapter 3 covers the experimental procedure, test set-up, and data analysis techniques. The results of this research are reported and analyzed in Chapter 4. Chapter 5 presents the conclusions drawn from this work as well as recommendations for future work.

II. LITERATURE REVIEW

Detonation research has been conducted since the late 19th century (5). Early research focused primarily on characterizing the detonation wave by using a one-dimensional model. From this one-dimensional model several key theoretical developments were made, including the Rankine-Hugoniot curve and the Zeldovich-von Neumann-Döring (ZND) model of the detonation wave (details are in Appendix A). Detonation research transitioned from this theoretical examination of the detonation wave to research regarding detonation engines. Both pulsed and rotating detonation engines have been studied, however, more progress was initially made regarding PDEs. Recently, though, there has been a renewed focus on RDEs.

2.1 Pulsed Versus Continuous Detonation Engines

A simple PDE is comprised of one or more combustion tubes that are filled with a nearly stoichiometric ratio of the fuel and oxidizer at the closed end of the combustion tube. A detonation is initiated near the closed end of the tube with subsequent wave propagation through the combustion tube toward the open end. The reactants initially propagate at subsonic deflagration speeds but eventually transition to supersonic detonation waves in a process known as deflagration to detonation transition (DDT). The residual hot gases are purged from the combustion tube in a blow down process. Pulse detonation engines operate cyclically (1). The feasibility of a PDE as a flight engine was proven on 31 January 2008, when a team from the Air Force Research Laboratory (AFRL) conducted a test flight of the first manned PDE-driven aircraft (Fig. 2).

Figure 2. First flight of PDE-driven aircraft

A rotating detonation engine is a relatively simple mechanical device that feeds propellants axially into an annular combustion chamber. The detonation wave propagates around the annulus of the combustion chamber near the propellant injector holes. The detonation wave does not exit the RDE as it would in a PDE. The detonation products flow axially downstream in the combustion chamber, following the bulk flow, and exit the open end of the combustion chamber. Unlike a PDE, RDEs have no check valve to ensure there is no back flow into the feed lines. Therefore, the propellant feed pressure must be high enough to prevent any hot detonation products from flowing back into the propellant lines. Additionally, the propellant feed pressure needs to be large enough to reestablish flow into the combustion chamber after the detonation wave has passed. The final restriction on the propellant feed pressure is that it must be high enough such that an adequate amount of combustible mixture has refilled the combustion chamber by the time the detonation wave has completed one revolution of the annulus.

2.2 Previous Continuous Detonation Engine Research

2.2.1 Rotating Detonation Wave Structure.

Some of the earliest research into rotating detonations focused on characterizing the structure of the detonation wave through a combustion tube (2). Research of this nature can be traced back to Russia in the late 1950s and early 1960s. During this time the work focused on the idea of a detonation wave propagating down the length of a cylindrical combustion chamber and spinning around the outer wall of the chamber in a helical trajectory.

One of the challenges of this early research was compensating for the discrepancy between the image velocity and the film velocity. Without correction, the slower film velocity resulted in images too distorted for practical use. However, the application of an absolute compensation method, in which the detonation wave is recorded by a camera set at an angle to a slit (this method is fully described in (2)), allowed for a clearer image of the spinning detonation.

Research has also focused on achieving continuous detonation in chambers of various geometries (3). One of the most commonly studied geometries for continuous detonation is an annular cylinder, shown in Fig. 3.

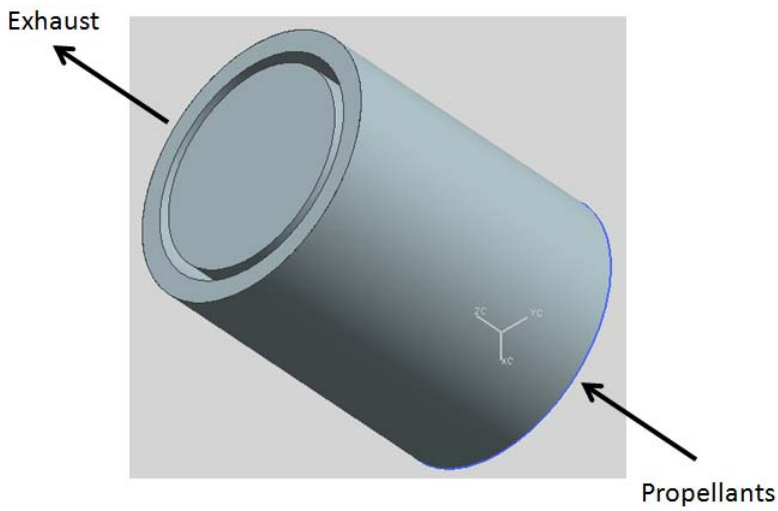

Figure 3. Annular cylinder combustion chamber

2.4.2 Computational Fluid Dynamics Work.

Both two-dimensional and three-dimensional CFD work has been done (4; 6; 7). Work at the Naval Research Laboratory (NRL) (4) focused on understanding the flow conditions within an RDE for premixed propellants. The RDE modeled had an outer diameter of 15 cm, a channel width of 2 cm, and a length of 17.7 cm. Their 3-D CFD model showed that with a small radial dimension of an RDE, compared with the azimuthal and axial dimension, the radial flow variation is minimal. This allows the engine to be adequately modeled in two dimensions, the azimuthal and axial dimensions. Figure 4, below, shows the expected flow structure of an RDE. The key features are the detonation wave (A), the oblique shock wave (B), the mixing region between the new and old detonation products (C), a secondary shock wave (D), the region of non-detonation burning that occurs at the interaction (E) between the fresh propellant (G) and the hot

products, and the high pressure region (F) just behind the detonation wave where the propellant inflow is temporarily blocked.

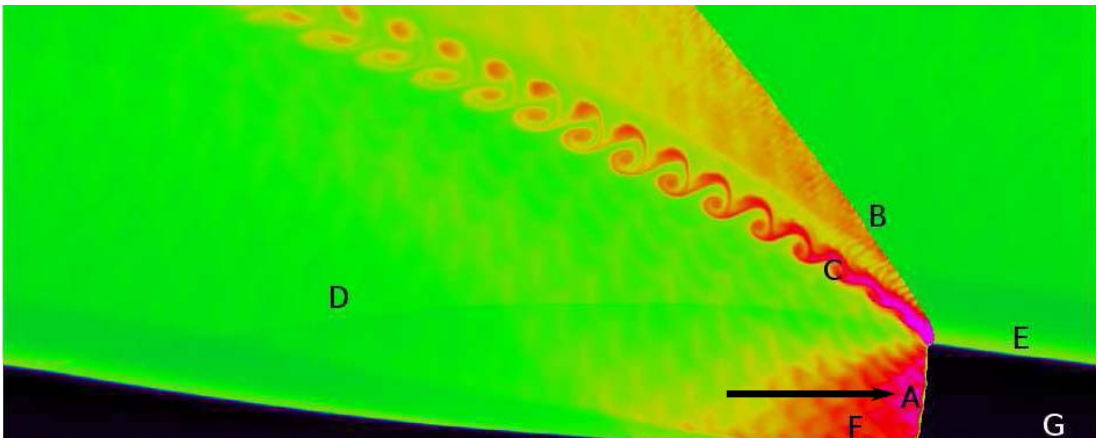

Figure 4. CFD model of rotating detonation wave structure (4)

Using the 2-D model created (Fig. 4), NRL researchers (4) examined the effects of the ratio of inlet stagnation pressure to back (exit) pressure (P_0/P_b) on detonation height, specific impulse, and the pressure ahead of the detonation wave using two methods. In one method, the stagnation pressure was held at a constant pressure while the back pressure was varied. In the other, the back pressure was held constant while the stagnation pressure was varied. They (4) found that for lower pressure ratios the detonation height, the height of the detonation front A in Fig. 4, increased as the pressure ratio increased. At higher pressure ratios, the detonation height was not affected by pressure ratio changes. They also found the specific impulse, or the change in momentum per unit amount of propellant used, increased with increasing pressure ratios. They (4) also found that the pressure in front of the detonation wave, in the region of unburned propellants, was dependent upon the stagnation pressure upstream of the

combustion chamber but relatively independent of the back pressure. An increase in stagnation pressure caused an increase in the pressure in front of the detonation wave whereas an increase in back pressure resulted in minimal change (4).

Additional CFD work, also both two- and three-dimensional models, has been done by the Japanese (6; 7). Their primary model was a Polish RDE with an outer diameter of 46 mm, channel width of 4 mm, and a length of 30 mm. The RDE was run with hydrogen and oxygen as the propellants. The purpose of this work was a sensitivity analysis of the RDE to reservoir pressure and temperature (6; 7).

2.4.3 Analytical Work

In addition to experimental and CFD work, analytical work has been done to determine the effect of various parameters on continuous detonation. Bykovskii et al. (3) determined the critical height (h*), the necessary height of the new layer of fresh propellants, may be related to the size of the detonation cell, λ, such that

$$\mathbf{h}^{*} \sim (\mathbf{12} \pm \mathbf{5})\boldsymbol{\lambda} \qquad \textbf{(}3\textbf{)}$$

and was found to agree with experimental data. Further, Bykovskii et al. related the minimum diameter of the outer wall of the chamber, $(d_c)_{min}$ to the detonation cell size such that

$$(\boldsymbol{d_c})_{\boldsymbol{min}} = \mathbf{28}\boldsymbol{\lambda} \qquad (4)$$

Bykovskii et al. also determined that the minimum channel width (Δ) was a function of the critical height of the propellants such that

$$\boldsymbol{\Delta \sim 0.2h^*} \tag{5}$$

Using their analytical relations for the diameter along with experimentally determined relations for the combustor length, Bykovskii et al. were able to obtain transverse detonation waves (TDW) for both acetylene-air and hydrogen-air mixtures. They also determined the range of existence for continuous detonation in fuel-air mixtures is a function of chamber pressure, ambient pressure, and air manifold pressure (3).

Additional work done by Bykovskii et al. (8) compared experimental results to the results obtained using mathematical models. They determined that the calculated pressure of the detonation was in agreement with the observed experimental pressure for hydrogen-oxygen mixtures. This experiment also allowed Bykovskii et al. to validate the previous estimation for the minimum propellant fill height, h* (8).

Further analytical work includes using mathematical models to determine the effect inlet Mach number has on the structure and range of existence for TDWs. Zhdan (9) focused on supersonic inlet Mach and determined that TDWs could be formed for an initial Mach number less than 3. However, there was no comparison to experimental data.

2.4.4 Previous Work on Hydrogen-Air Systems

A significant amount of experimental work with RDEs is done using oxygen rather than air as the oxidizer (6; 8). However, some work has been done on systems

using hydrogen and air as the propellants (10; 11). Russian researchers (10) have obtained detonation using hydrogen-air in an RDE with a diameter of 30.6 cm (approximately 12 inches) and a channel width of 2.3 cm (0.91 inches). They were able to obtain detonation wave speeds on the order of 1,100 m/s to 1,430 m/s, corresponding to frequencies of 1.15 kHz to 4.46 kHz, for equivalence ratios of 0.8 to 1.94. The effect of mass flow rates on the system was also examined. They found that higher mass flow rates yielded more transverse detonation waves.

In addition to the Russian work, Polish researchers (11) obtained detonations using hydrogen and air as propellants in an RDE with a diameter of 150 mm (approximately 6 inches) with a 10 mm (0.39 inches) channel width. The experimentally observed detonation waves propagated with a velocity of 1,410 m/s, corresponding to the detonation velocities observed by Russian researchers (10). Polish researchers (11) also obtained pressure traces with three probes placed along one cross-section of the engine.

2.4.5 Previous Air Force Research Laboratory Work

Previous (to the author) work done at AFRL's Detonation Engine Research Facility (DERF) includes the build-up and initial testing of an RDE on loan to the Air Force from Pratt-Whitney. The initial testing included cold-flow tests to ensure the controls were working correctly and to estimate the detonation cell size, λ. The detonation cell size is important since the necessary height of the fresh propellants for sustained detonation is directly related to the cell size (12).

The first cold-flow tests, conducted with only standard air, showed a negative pressure within the channel, most likely due to over-expanded, supersonic flow. Tests were also conducted with both fuel (helium) and standard air. Rather than venting

stoichiometric amounts of flammable propellants into the test chamber, helium was used for the fuel in place of hydrogen. Helium was chosen because its Reynolds number matches hydrogen within 1%. When this test was conducted, a negative gage pressure was again seen when the air valves opened. However, when the fuel valve was opened, the chamber pressure increased by approximately 1.5 psig, as shown in Fig. 5. Since helium is lighter than hydrogen and has a higher specific heat ratio, γ (1.66 compared to 1.41), the local speed of sound was increased, causing the flow to be less over-expanded than the air only cold flow tests (12).

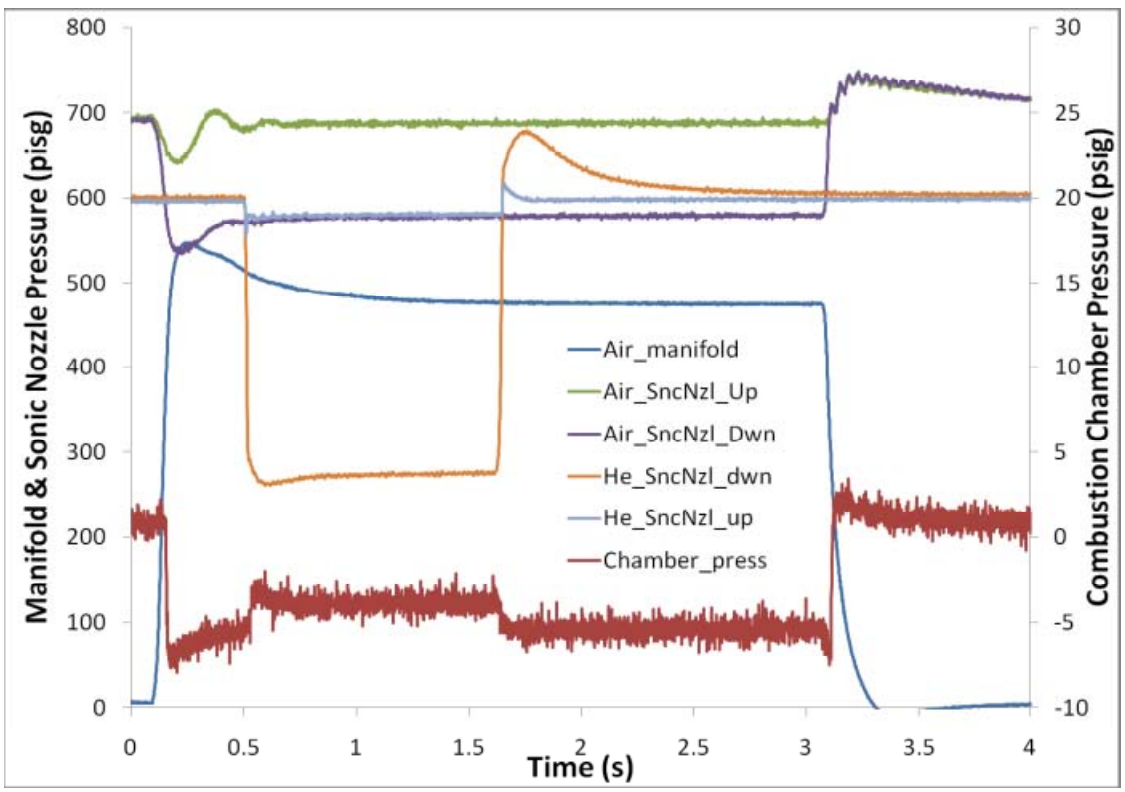

Figure 5. Cold flow data for helium-air test (12)

Based on these results and published data relating the initial pressure of hydrogen to the detonation cell size, λ, an estimate for cell size was extrapolated. For the pressure associated with the helium-air test, an estimated cell size of 12 mm was obtained (12).

III. FACILITY AND TEST SETUP

3.1 Detonation Engine Research Facility

Experiments were performed in the Detonation Engine Research Facility (DERF) located in Building 71A, D-Bay, Wright-Patterson Air Force Base, Ohio (D-Bay). D-Bay is a part of the Air Force Research Laboratory Propulsion Directorate, Turbine Engine Division, Combustion Branch (AFRL/RZTC).

D-Bay consists of the test cell, control room, fuel room, and compressor room. To protect personnel during tests, the 21,200 m^3 (748,670 ft^3) explosion proof test cell is surrounded by at least 0.61 m (2 ft) of reinforced concrete. The test cell contains a test stand upon which the PDE is mounted. Both the RDEs are mounted beside the test stand.

All the equipment necessary for remotely operating the engines and collecting data is located in the control room. The engines may be visually monitored via closed circuit cameras. The RDE is controlled by both the control panel and the control computer. The control panel contains the physical switches for the power supply and valves for the fuel, oxidizer, and pre-detonator lines. Physically turning off a switch removes power to that system, preventing the RDE from firing regardless of commands from the control computer. The control computer uses *LabView*® as the control software. The control program monitors low speed (kHz) data such as the fuel and oxidizer line pressures at various locations, as well as the load cell pressure data. High speed data is collected using a *LabView*® program capable of recording data from 16 channels at rates of up to 5 MHz on the data collection computer. This high speed data collection system is used to obtain pressure data. The high speed data is analyzed after

testing is complete, but a limited amount of analysis may be done between runs using the software in order to verify that the sensors are working correctly (13).

3.2 Engine Setup

The RDE used in these experiments, shown in Fig. 6, was originally designed and built by Pratt-Whitney, Seattle Aerosciences Center. Pratt-Whitney conducted some preliminary tests with this engine using ethylene and oxygen as the propellants. Little is known about the tests they conducted, however, after a catastrophic failure, the engine was retooled and loaned to AFRL.

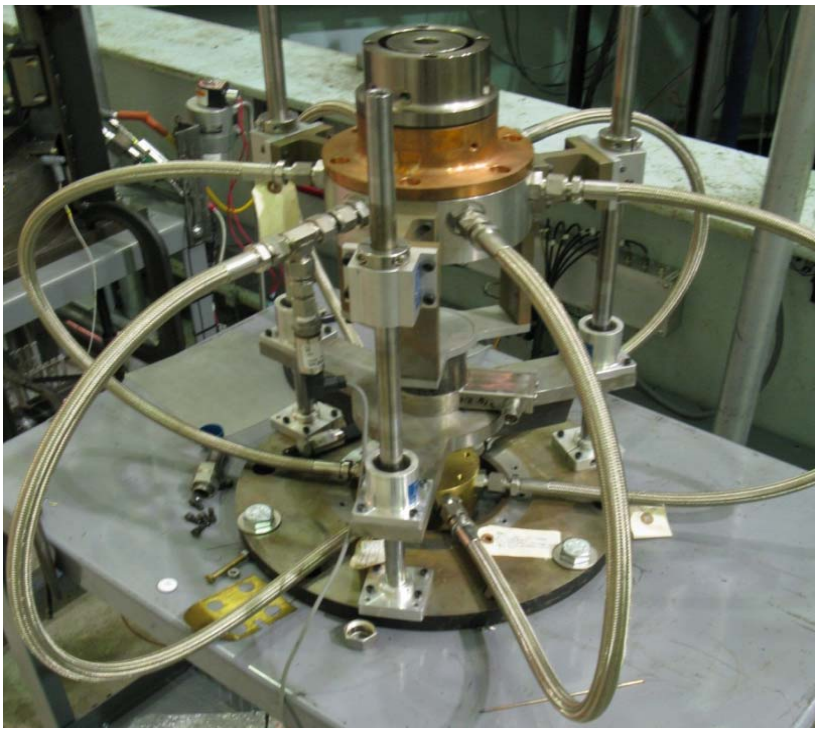

Figure 6. Pratt-Whitney rotary detonation engine

The combustion chamber is composed of two sections. The lower section, which contains the detonation plane, is made of copper while the upper section is made of steel. The combustion chamber has a 0.0762 m (3 in) outer diameter and is 0.1016 m (4 in) in length. The combustion channel width is controlled by the diameter of the steel center-body. Three center-bodies are available which yield channel widths of 2 mm, 6 mm, and 10 mm, respectively. The fuel, hydrogen for the experiments done, enters the engine from a single fuel line at the center of the engine's base. The oxidizer, air, enters the air manifold and is divided and ducted to the engine via six lines. The feed pressures are listed in Table 1. The propellant feed pressures are so high in order to prevent the high pressure region behind the detonation front from creating reverse flow into the propellant lines.

Table 1. Propellant feed pressures

Standard air sonic nozzle diameter (in)	Feed pressure (psig), high	Feed pressure (psig), low
0.201	812	256
0.252	744	210
0.315	693	455
Enriched air sonic nozzle diameter (in)	Feed pressure (psig), high	Feed pressure (psig), low
0.201	565	287
0.252	729	322
Hydrogen sonic nozzle diameter (in)	Feed pressure (psig), high	Feed pressure (psig), low
0.063	585	90
0.125	561	90

The propellants enter the base of the combustion channel through choked orifices. Figure 7 is a schematic of the propellants entering the combustion channel.

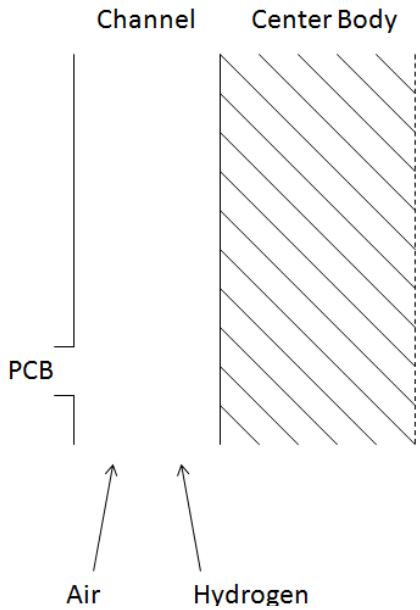

Figure 7. Schematic of RDE

A detonation is initiated tangentially to the flow via a spark plug initiated pre-detonator. The detonation wave travels circumferentially around the combustion chamber and the detonation products are exhausted through the open end of the chamber. A ring of three PCB® dynamic pressure transducers is located on approximately the same plane as the pre-detonator. The three PCBs are spaced 120° apart. Pressure data was sampled at 2 MHz. The data collected from the PCBs was used to determine both the velocity of and the direction of the combustion front. Figure 8 shows the propellant lines and flow direction as well as the location of the PCBs and the pre-detonator.

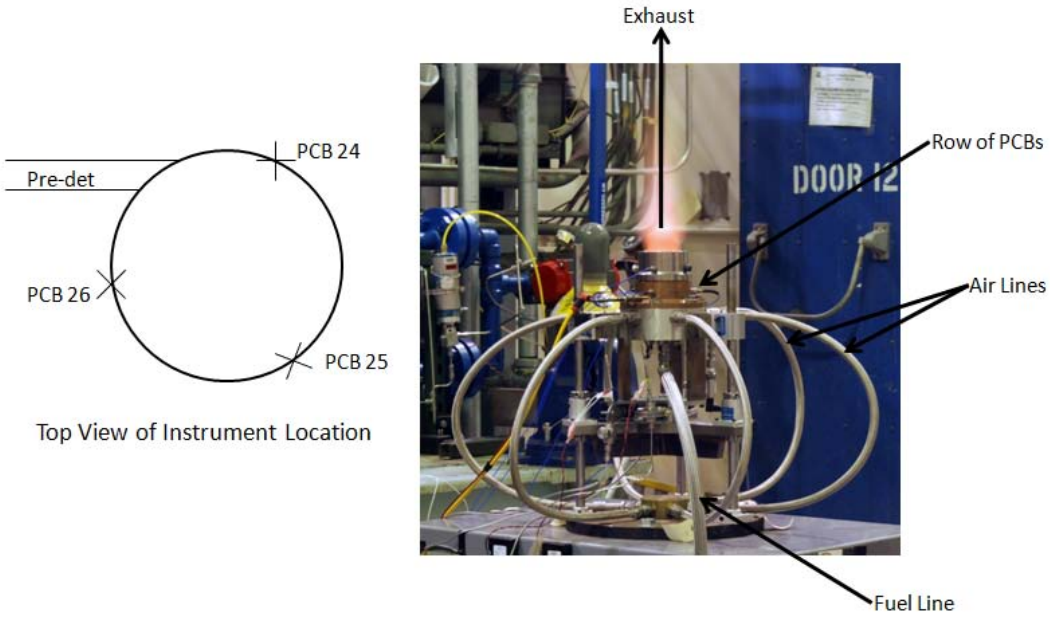

Figure 8. Instrumentation and propellant flow direction.

The propellants are delivered to the RDE through a series of manual valves, sonic nozzles, and check valves. The mass flow rates of the propellants are controlled by dome-loaded pressure regulators and sonic nozzles. Fast-actuating, air-driven valves quickly turn on and off the propellant flow during runs. Figure 9 illustrates the propellant delivery system.

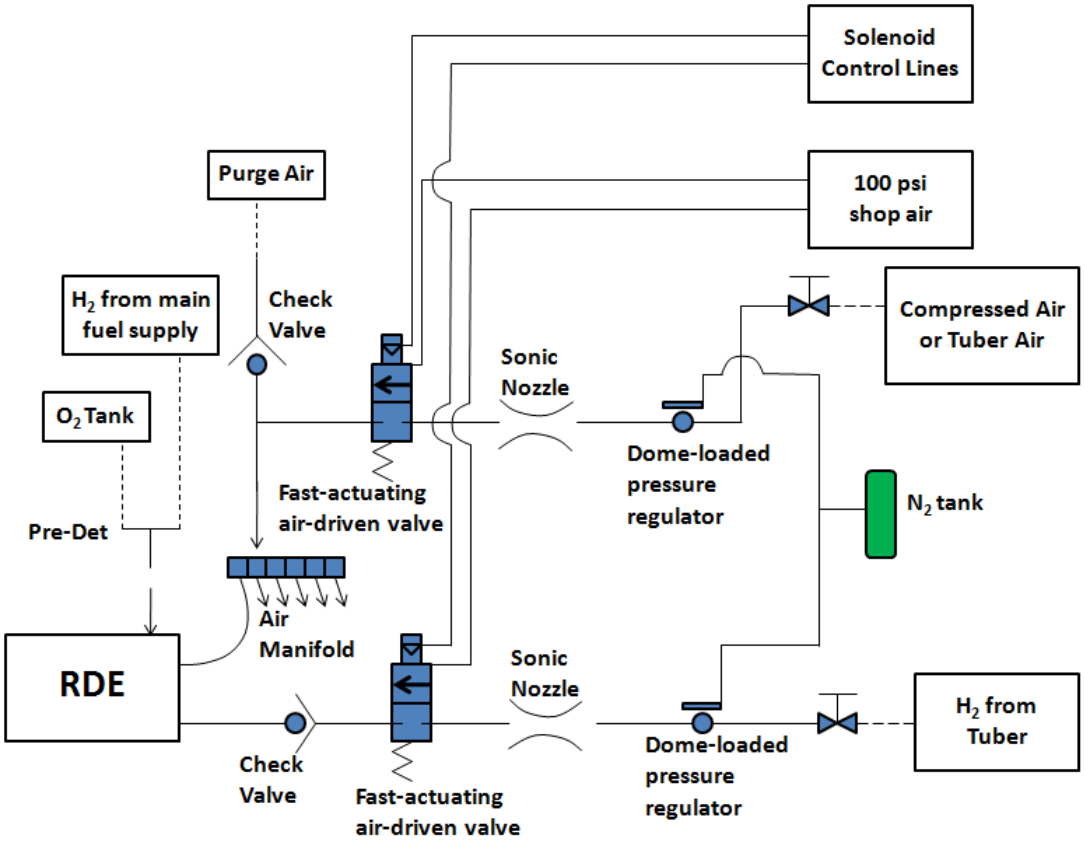

Figure 9. Propellant delivery system

For a given run, the *LabView*® control program collects data for 5 seconds. The air valves are opened and the air is allowed to stabilize for approximately 1.5 seconds prior to the pre-detonator fire command. The hydrogen valves are opened and the hydrogen is allowed to stabilize for 0.55 seconds before the pre-detonator fires. After the pre-detonator is fired at a time of 1.5 seconds, the hydrogen and air continue to flow for 0.75 seconds. The actual run event begins at 1.5 seconds and is completed at approximately 2.4 seconds. Figure 10 shows the data collected using *LabView*®. The *LabView*® control program operates all the valves so the timing of the run sequence is

the same for each test. High speed data from the PCBs is collected for the 1 second beginning with the pre-detonator fire command.

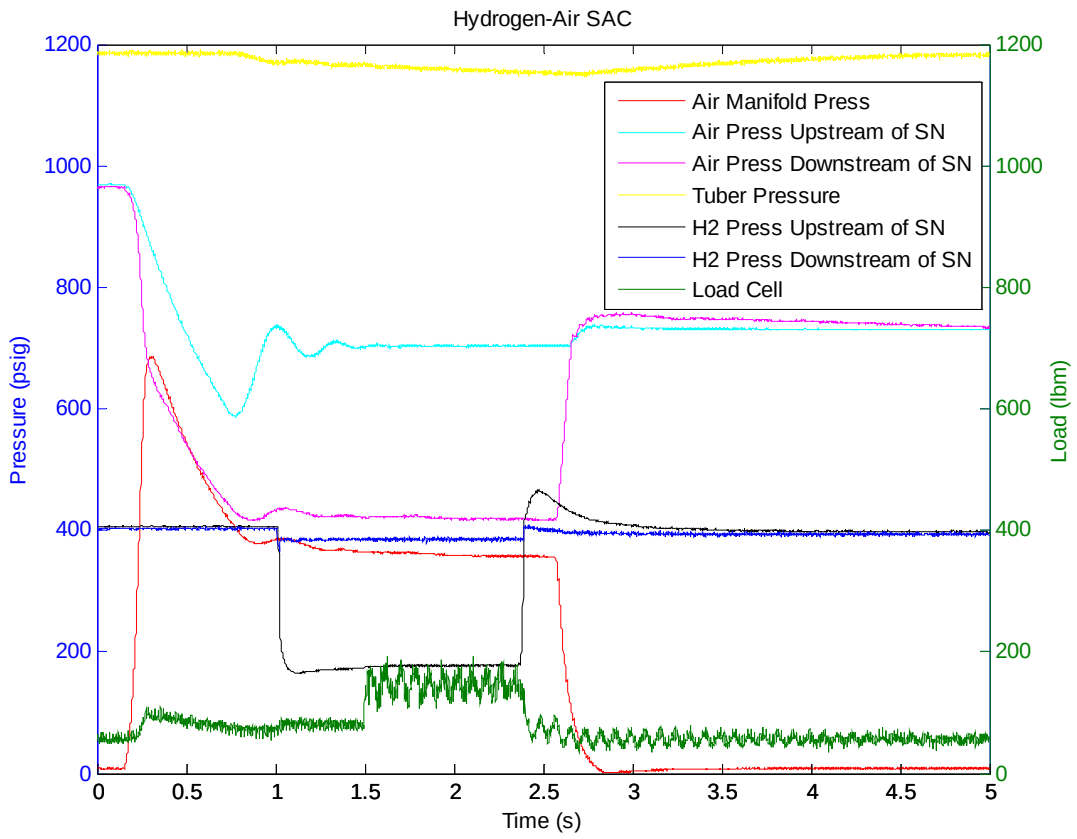

Figure 10. Sample low-speed data acquired by LabView®

Four parameters can be varied to control engine operation, including mass flow rate, equivalence ratio, channel width, and size of the choked orifices. Of these four parameters, mass flow rate and equivalence ratio were the primary variables for the tests in this report. Data from static pressure transducers located upstream of the sonic nozzles

was collected at 1 kHz and used to determine the mass flow rate and equivalence ratio for each run.

3.3 Air Supply

Two sources of air were available for use with the RDE. The first air supply is a compressed air tank located behind D-Bay. The air supply from this tank is “standard” air with approximately 21% oxygen and 79% nitrogen. The second air supply is a tuber trailer of “enriched” air. The enriched air is comprised of approximately 23% oxygen and 77% nitrogen. The percentage of oxygen and nitrogen in the air supply affects the detonation cell width which directly affects the height of fresh propellant necessary to sustain detonation (Eq. 3). Using data obtained from the detonation database (14) for hydrogen-oxygen with nitrogen dilution, a chart of hydrogen-oxygen with varying percent nitrogen versus cell width (mm) was created (Fig. 11) and a second order polynomial fit of the data was used to extrapolate the data to 77% and 79% nitrogen dilution. This showed that for an increase in nitrogen of 2%, the cell width increases from 12.6 mm to 13.3 mm. Data for hydrogen-oxygen with nitrogen dilution was used because no data was available for air with 23% oxygen. Data for the cell size of standard air as a function of equivalence ratio and pressure exists, but this yields no correlation to an air with a higher percentage of oxygen.

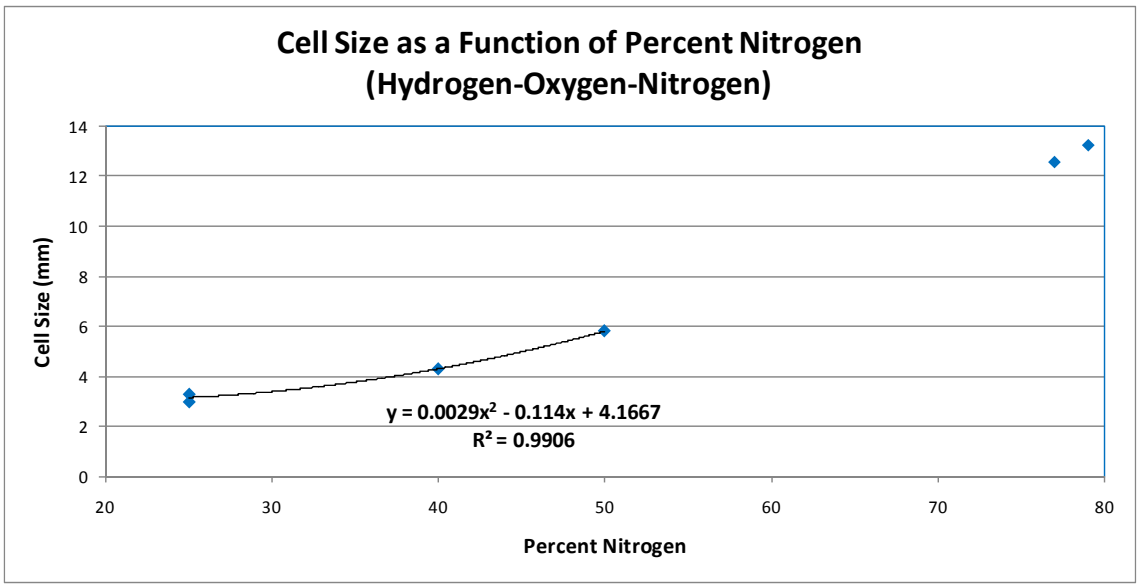

Figure 11. Cell width as a function of percent nitrogen

Tests were conducted using both standard and enriched air. All tests conducted with the enriched tuber air were done using the 6 mm channel. Runs conducted using standard air utilized all three channels.

3.4 High Speed Video Footage

Video footage of the tests was desired in order to verify that detonation occurred, to help visualize flow in the chamber and to record the number of detonation waves present during each run. In order to avoid damaging the high speed Phantom 7.1 camera, a mirror was mounted over the Pratt RDE rig to allow indirect visualization of the runs (see Fig. 12). The mirror mount was constructed by attaching unistrut to the existing fire suppression system. The mirror was attached to this assembly via the head of a tripod mount. A tripod mount was used because the head has three degrees of motion allowing the mirror to be adjusted and locked into place. The mirror was placed on the tripod

mount by an assembly of smaller pieces of unistrut attached to the mirror with doubled sided foam tape.

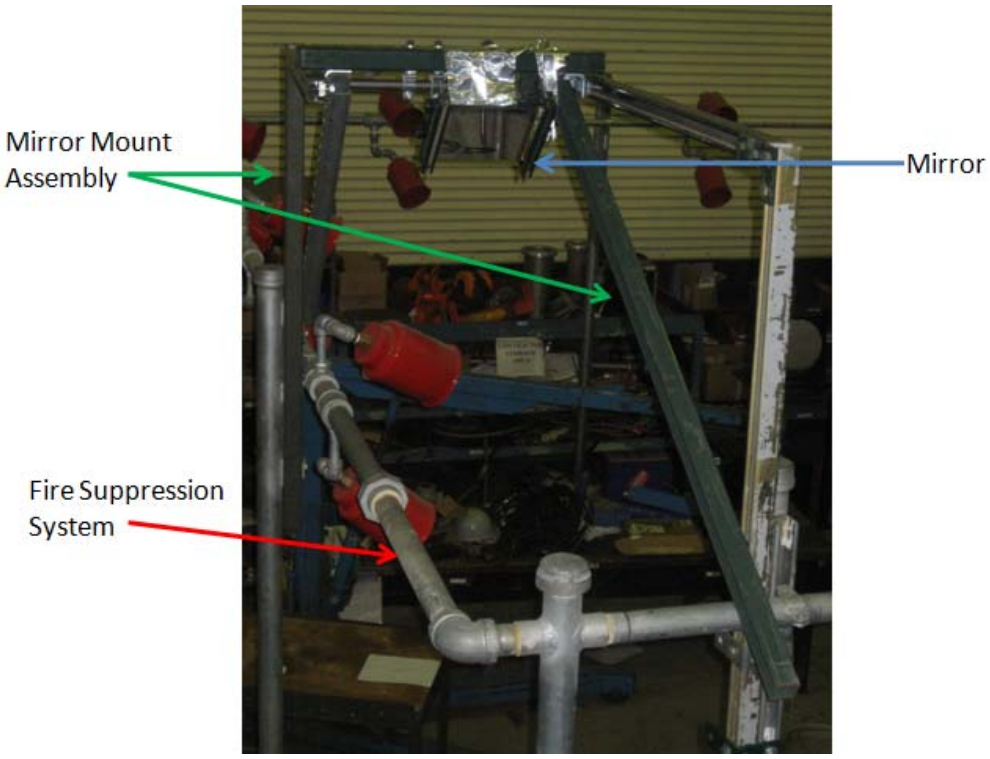

Figure 12. Mirror mount assembly

The mirror is a flat first surface glass rectangular mirror 6” tall, 9” in length, and 0.25” thick. A first surface mirror was chosen for better optics. The mirror has greater than 90% reflectance in the visible spectrum and was allowed to have less than 0.7 mm pinholes and 0.08 mm scratches as long as they were shorter than 1/3 the length of the longest edge. While higher quality mirrors are available, they were not required since no quantitative data was to be obtained from the images.

Video of the tests was collected at 50,000 frames per second, with a 15 μs exposure time, and at a resolution of 128 by 128 pixels. After the camera was triggered, 38,745 frames were collected. The detonation front was expected to travel around the annulus between 5,000 and 8,000 times per second. The frame rate was chosen in order to completely capture the detonation wave front.

3.5 Successful Run Criteria

A run was considered successful if the detonation remained in the channel for the duration of the run (0.9 sec or longer) and was repeatable. A few different methods were used to determine if the run stayed in the channel for the full 0.9 sec. The primary validation was whether or not pressure data was collected for 0.9 sec. Figure 13 shows a pressure trace for a run which stayed in the channel for the full 0.9 sec. It is clear that data was collected for the duration of the run. Figure 14 shows the pressure trace for a run which did not remain in the channel for the full 0.9 sec. Pressure data was collected for the length of time the detonation event was in the channel (approximately 0.125 sec in this case). Once the detonation event was no longer in the channel, no data was collected, as is indicated by the lack of pressure spikes seen after about 0.125 sec in Fig. 14.

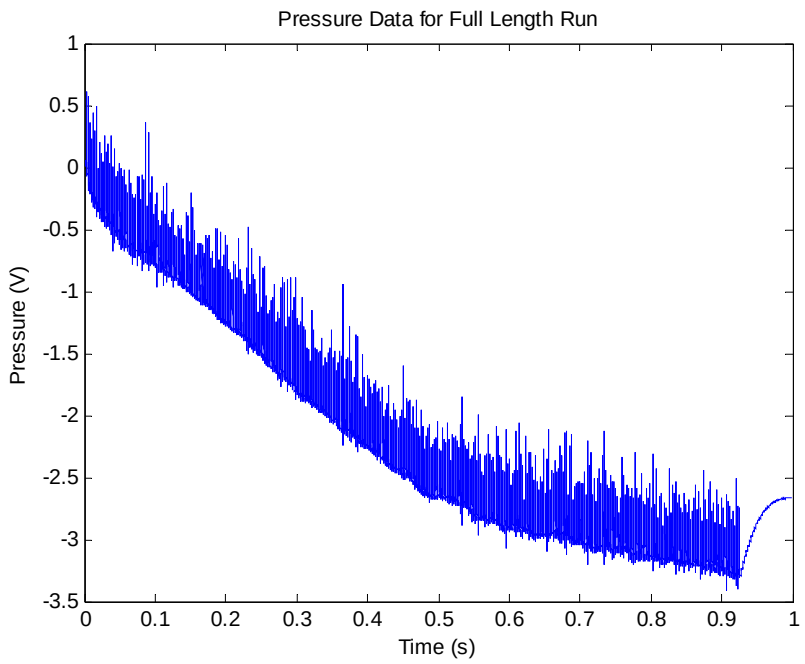

Figure 13. Pressure trace for a full-length run

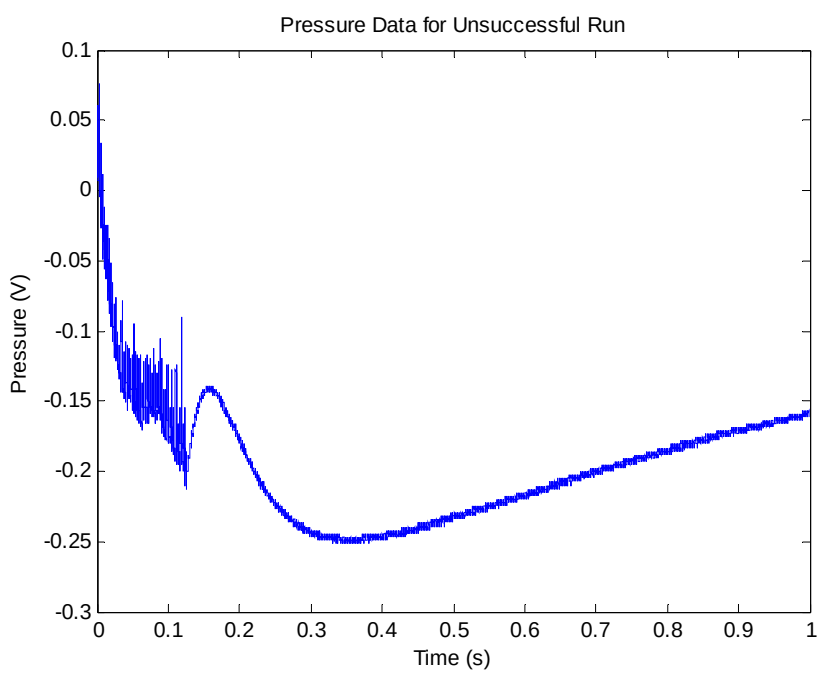

Figure 14. Pressure trace for a run that did not stay in the channel

During the actual test, visual and audible methods were used as additional verification that the detonation event did not stay in the channel for the full run. If the detonation event stayed in the channel, the exhaust plume was small and the engine sounded a certain way. If the detonation event did not stay in the channel, the exhaust plume was much larger and the engine had a different sound. A run in which the detonation event stayed in the channel for the full 0.9 sec met all three of these verification methods; that is, pressure data was collected for the full run, the exhaust plume was small, and the engine sounded "correct." However, if the detonation did not remain in the channel for the full 0.9 sec, none of these verification methods were present; i.e. pressure data was not collected once the detonation was no longer in the channel, the exhaust plume was large, and the engine sounded "wrong." If the detonation did not remain in the channel for the full run, the specific set points (mass flow rate and equivalence ratio) would be of little use in future runs where a longer duration could be desired. Run time was restricted to 0.9 sec by choice. Because the engine was not cooled during the actual run event, a limited run time helped ensure the instrumentation was not damaged during testing.

Runs were usually conducted within 5 min of each other. In between runs, air flowed through the engine for cooling purposes. Three runs were conducted for each set point. For set points which were not repeatable, no discernable order was noticed. Sometimes the successful run was the first run conducted, other times it was the middle run, and other times it was the final run conducted.

3.6 Data Collection

Three primary methods were used to collect data for each run. The control program recorded the tank pressures, line pressures, load cell data, and shell temperature

at a rate of 1 kHz for 5 sec. The pressures upstream of the sonic nozzles were used in the calculation of mass flow rate and equivalence ratio. High speed video footage was also recorded.

The dynamic pressures seen by the PCBs were recorded by the high speed data collection computer at a rate of 2 MHz for 1 sec beginning with the pre-detonator fire command. The times between the peaks of this pressure data were used to calculate the velocity of the combustion front. Thus, accurate timing was more important than accurate pressure measurements, and for this reason, PCB® Piezoelectric Dynamic Pressure Transducers were used. The PCBs have a response time of less than 1 μs. If the detonation front was travelling at a CJ velocity of 1950 m/s, this would correspond to a frequency of 8.1 kHz, corresponding to a time of 123 μs. A rise time of less than 1 μs decreases the likelihood of the sensor missing a pressure spike or recording the pressure spike at an inaccurate time. As this is a response time, it follows that the sensor should drop back to its zero value within 1 μs of the detonation wave passing. However, PCBs only record the pressure of the spike to within 1% of the full range (5000 psi) of the sensor. As the pressures generated by the detonation front were on the order of 300 to 500 psi, an accuracy of +/- 50 psi yields a large bias error. If more accurate pressure measurements are required, Kulite® sensors would provide increased accuracy for the pressures at the cost of the accuracy of the timing.

3.7 Data Reduction

Several different methods were used to verify the run velocities. The first method is a time of flight code in MatLab®. The code calculates an average of the raw pressure

data and then searches for pressure peaks. A peak is defined as three points in a row which lie above one standard deviation above the mean. Once a peak is found, a hold of 100 μs is initiated (explained momentarily) which prevents the time of flight code from searching for another peak until the hold time has passed. This prevents the code from double counting a peak. Figure 15 illustrates this hold time. In the figure, a peak is found at point 1 and a 100 μs hold is initiated. The hold ends at point 2 and the code begins searching for another peak. A second peak is found at point 3 and the cycle begins again.

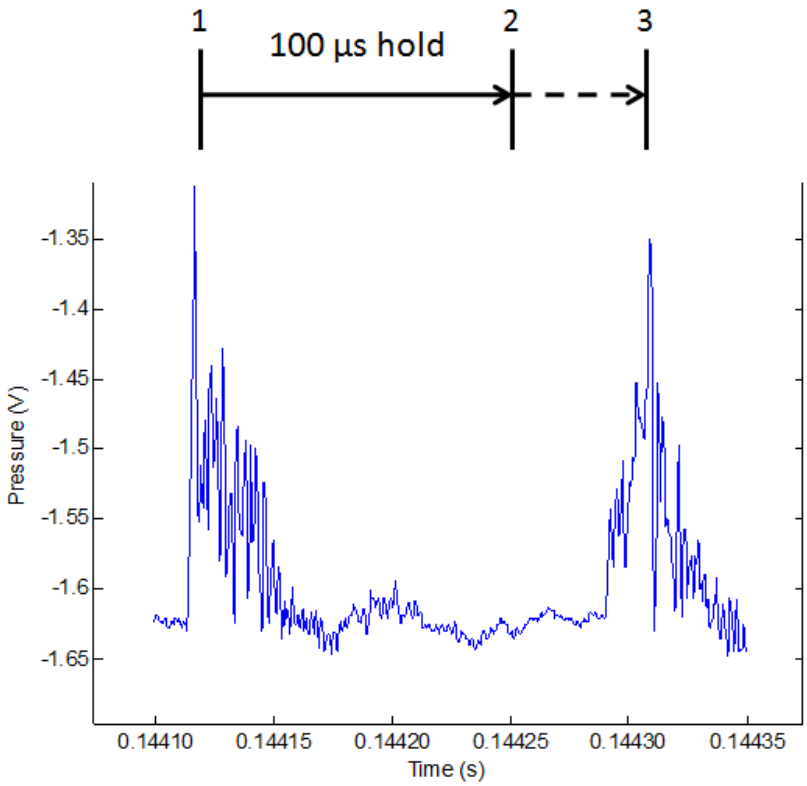

Figure 15. Time of flight code hold time

The choices for these three parameters, the number of points above the threshold, the pressure threshold (number of standard deviations above the mean), and the hold time are relatively arbitrary. A sensitivity analysis was done using data from two different runs in order to verify the choices listed above. In the sensitivity analysis, the number of points above the threshold was varied from 1 to 4, the threshold was varied from 0 to 2 standard deviations above the mean, and the hold time was varied from 60 to 120 μs in 20 μs increments. The average run velocities for a single PCB were calculated as these parameters were varied. The full tables of data from the two runs examined are shown in Appendix B. One graph for each threshold was generated in order to examine the effect of hold time and number of points above the threshold. From Figs. 16-18, it is clear that hold times of 60 and 80 μs yield the most variation as the number of points above the threshold changes for thresholds of 0 and 1 standard deviations above the mean.

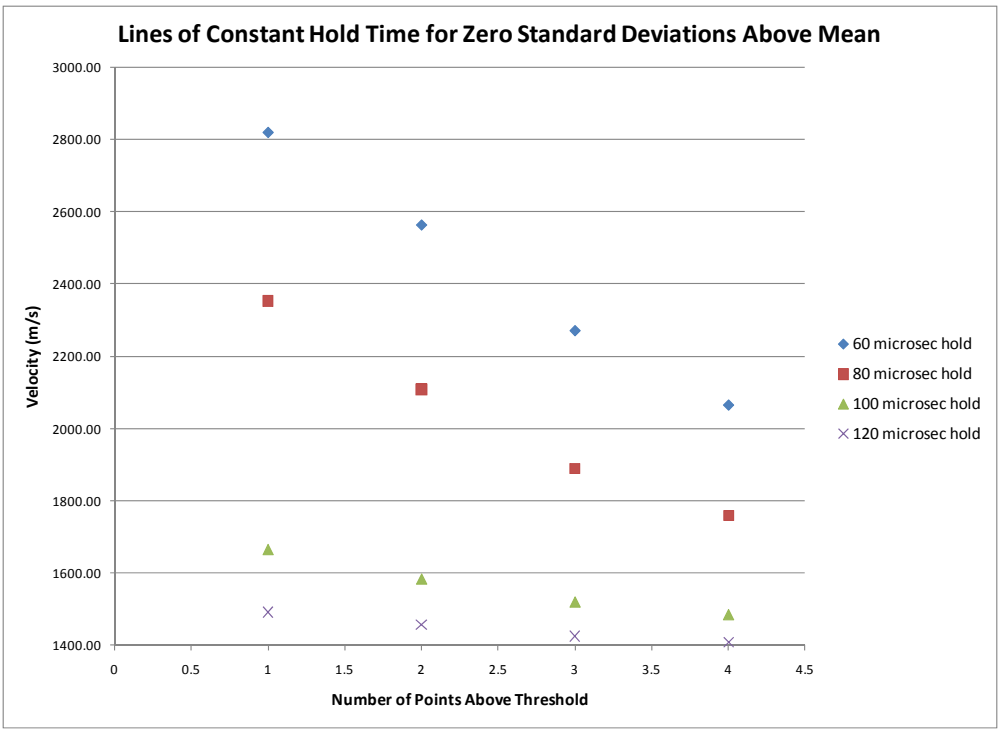

Figure 16. Zero standard deviations above the mean

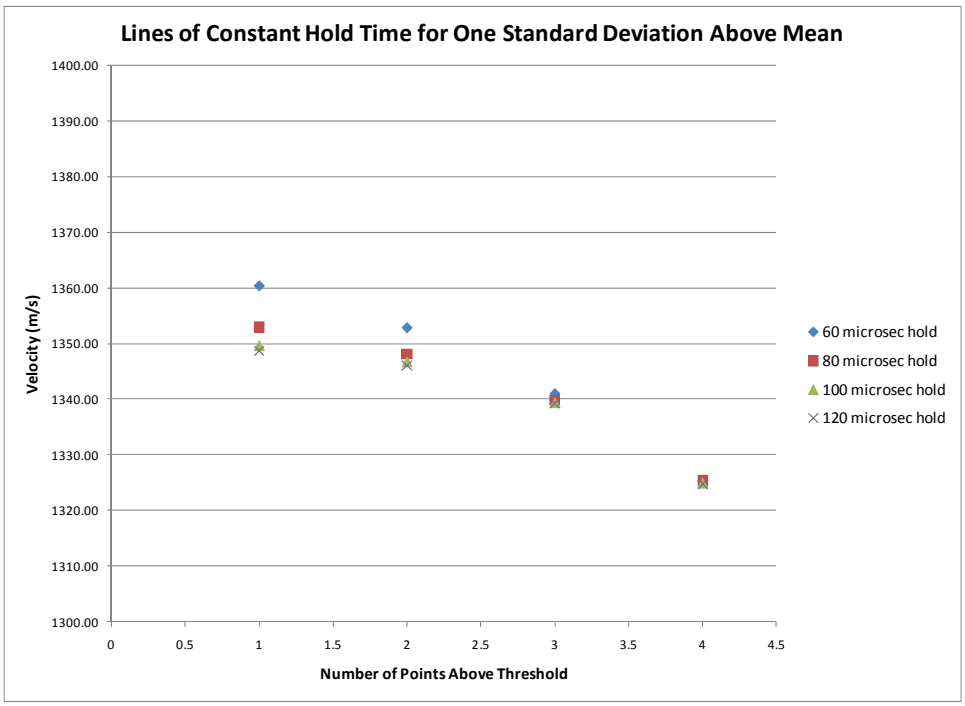

Figure 17. One standard deviation above the mean

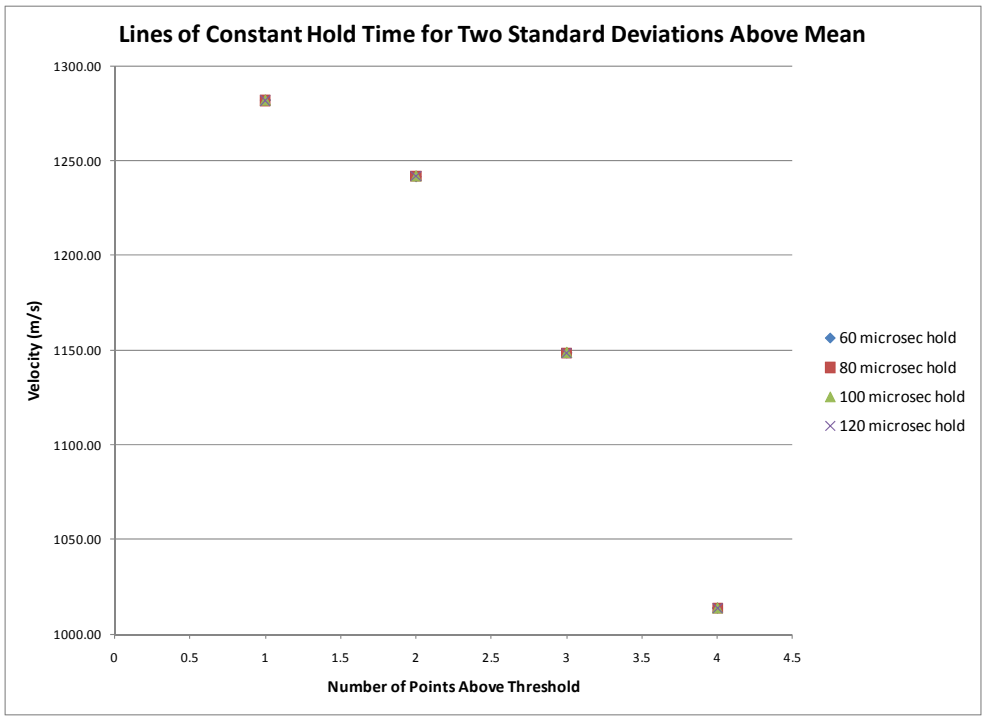

Figure 18. Two standard deviations above the mean

Given the large variation seen at 60 and 80 μs hold times for thresholds of zero and one standard deviations above the mean, all points corresponding to hold times of 60 and 80 μs were removed and a graph of all three thresholds with hold times of 100 and 120 μs was created (Fig. 19).

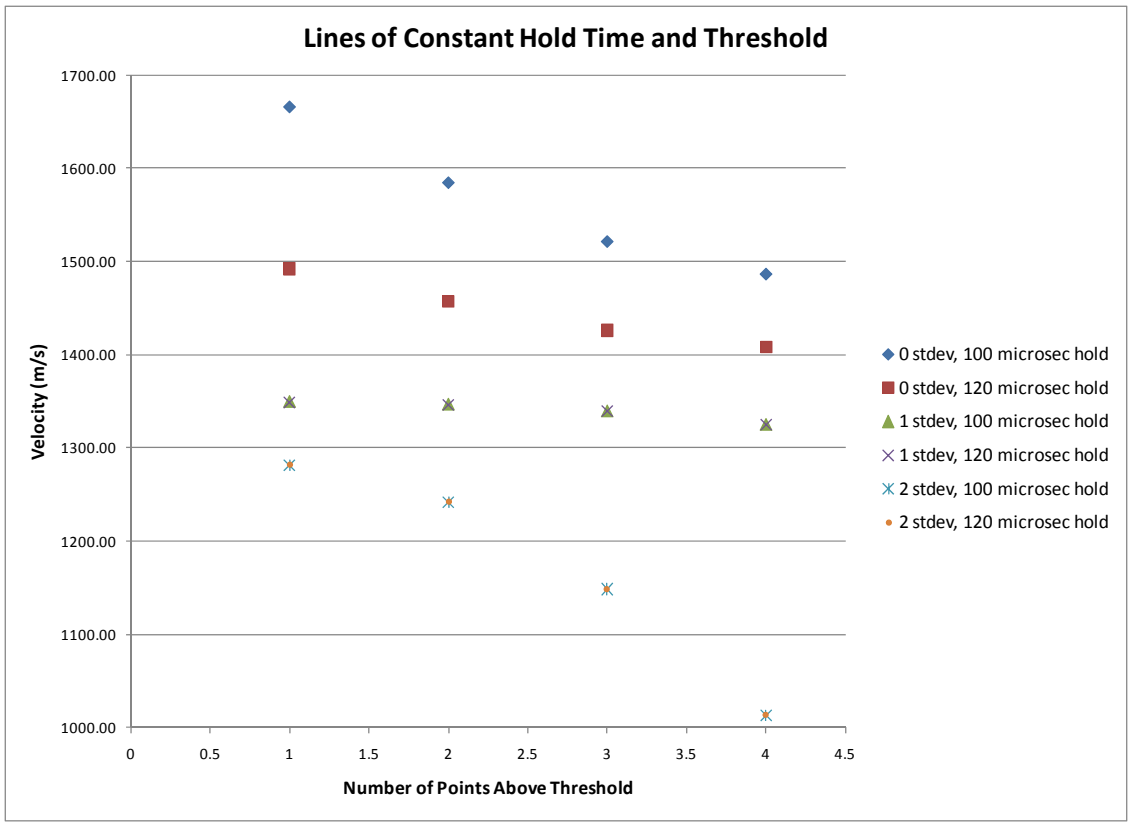

Figure 19. Final parameter comparison

From Fig. 19it is clear that the least variation in velocity occurs for a threshold of 1 standard deviation above the mean. There is virtually no variation in the velocities when the hold time is increased from 100 to 120 μs (less than 1 m/s variation for a given number of points above the threshold). A hold time of 100 μs would correspond to a maximum velocity of 2400 m/s while a hold time of 120 μs would correspond to a maximum velocity of 2000 m/s. Since the CJ velocity is 1950 m/s, a hold time of 100 μs was used since it corresponds to a slightly higher maximum velocity. The final parameter is the number of consecutive points above the threshold. The number of consecutive points above the threshold is used to determine the percent probability that

the code will return an erroneously high velocity. Since the threshold is 1 standard deviation above the mean, the percent probability of an erroneously high velocity is calculated as 0.17^x, where x is the number of consecutive points above the threshold. Three consecutive points above the threshold was chosen because this yields a 0.5% probability of an erroneously high velocity while yielding an average velocity that varies less than 1% from the average velocities found using 2 and 4 consecutive points above the threshold.

For each of the three PCBs, the time of flight code calculates velocities between subsequent peaks and returns a graph of the velocities as a function of the time at which they occur as well as the average run velocity. An example of the velocity graph is shown below in Fig. 20. Further examples are available in Appendix C.

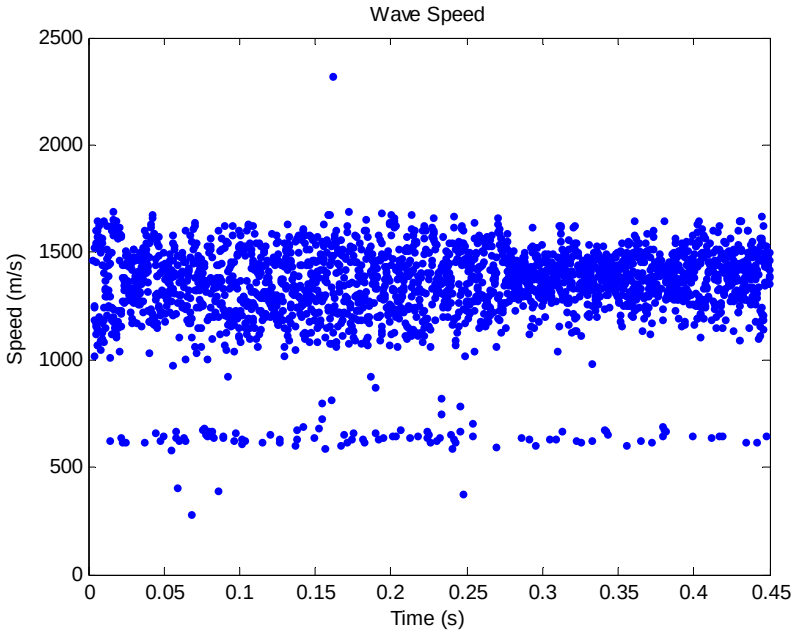

Figure 20. Velocities for PCB 24 from time of flight code

From Fig. 20, it is clear that the velocity varies as the run progresses, with a primary band of velocities centered around approximately 1400 m/s and a secondary band of velocities centered around 600 m/s. During this time span the flow reverses and the lower band may be an artifact of the reversal event. More study is planned to determine the cause of the lower band. Hayashi et al. (6) also saw two distinct bands of velocities in their experiments (Fig. 20). They did not explain the second band.

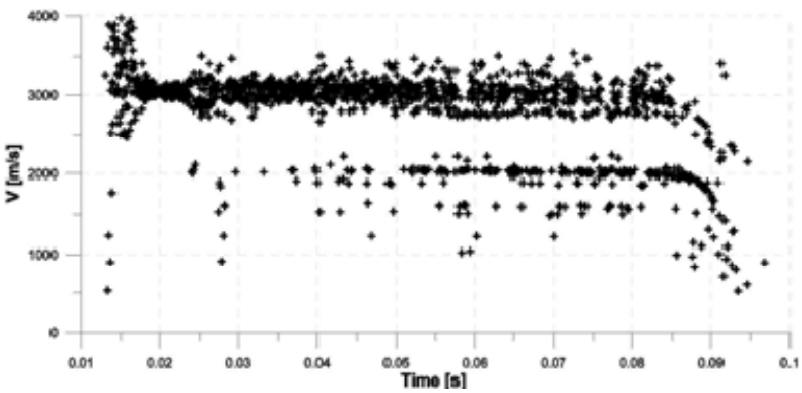

Figure 21. Velocity graph of hydrogen-oxygen run (6)
(poor quality original)

The author used another method to verify the varying velocities seen in Fig. 20. The raw pressure data for all three PCBs was plotted on one figure, shown in Fig. 22Figure **22**.

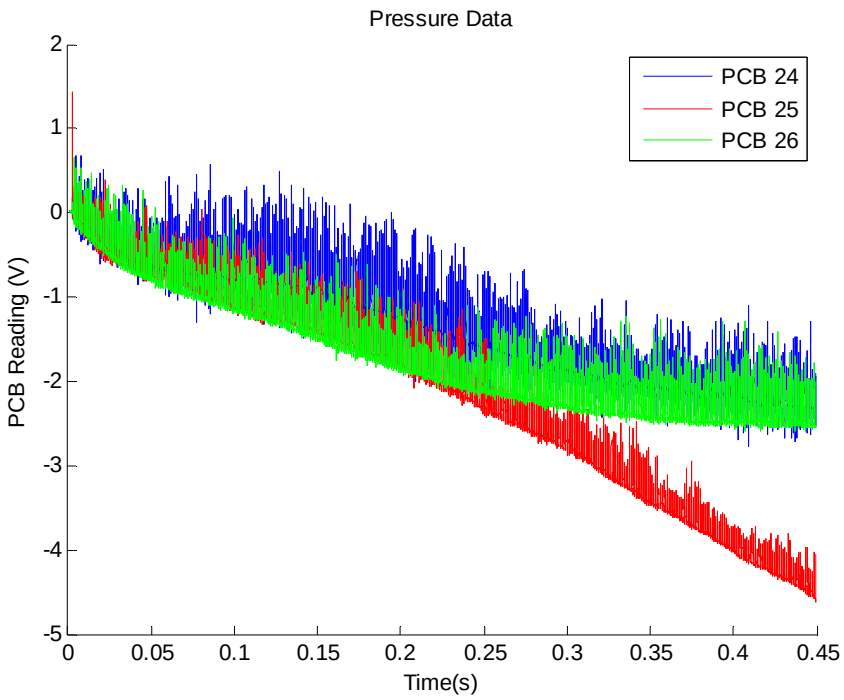

Figure 22. Raw pressure data

By focusing on a small section of the data, the pressure peaks are resolved well enough that it is possible to determine the times for the peaks. From these times, it is possible to calculate the velocities between peaks for a single PCB and between subsequent PCBs. This process was not automated because the direction in which the detonation wave propagates reverses periodically throughout the run. It is therefore important to note the order in which the pressure spikes occur when calculating the velocity between two different sensors. The velocities calculated for peaks between a single PCB all lie within the two velocity bands seen in Fig. 20Figure **20**. Although the velocities calculated between sequential PCBs may lie outside of these bands, the average velocity of this data falls within the bands.

Figures 23-25 illustrate this direction reversal and regions of higher and lower velocities. Following the PCB order (24, 25, 26 in a clockwise direction, as seen in Fig. 7), a clockwise direction would be indicated by a sequence of blue-red-green (PCB 24-25-26). In Fig. 23, the sequence is green-red-blue (PCB 26-25-24) and is indicative of a counter-clockwise flow. In Fig. 24, the sequence is green-red-blue (PCB 26-25-24) until just prior to 0.055 seconds at which point the sequence changes to blue-red-green (PCB 24-25-26). This sequence change corresponds to a direction change. The sequence in Fig. 25 is blue-red-green (PCB 24-25-26), indicating a clockwise flow. The pressure peaks in the region around 0.0685 seconds in Fig. 25 are farther apart than the peaks in the range of 0.069 to 0.07 seconds. Lower velocities would therefore be seen in the region around 0.0685 seconds and higher velocities would be seen in the range of 0.069-0.07 seconds.

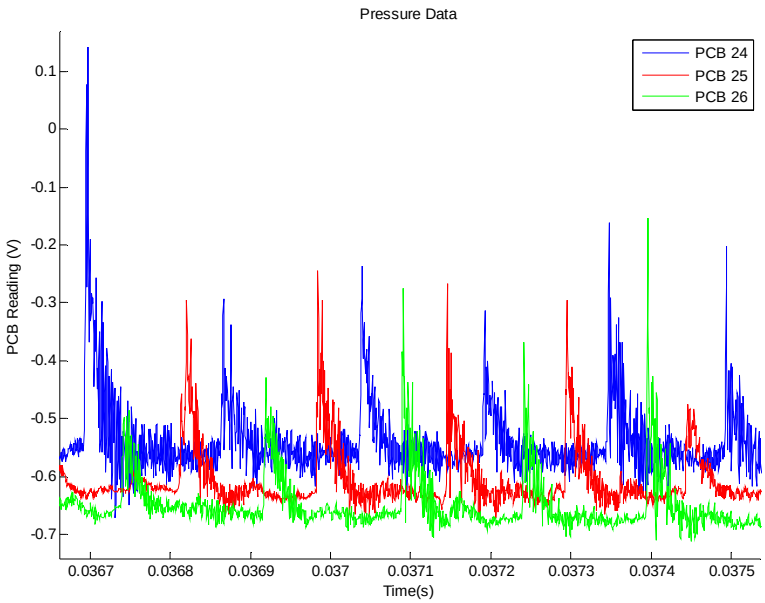

Figure 23. Close up view of Fig. 22, counter-clockwise flow (PCB 26-25-24)

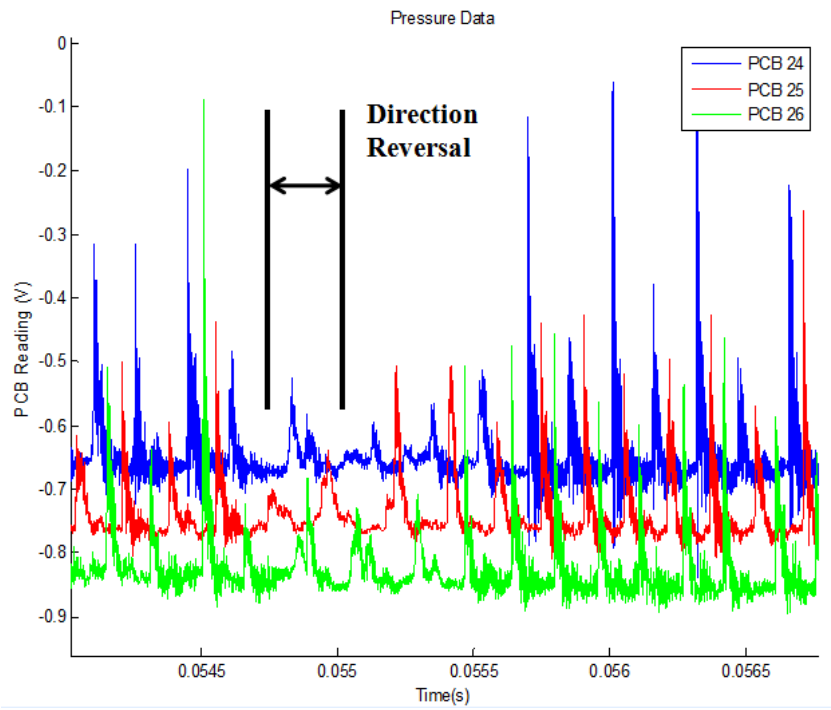

Figure 24. Close up view of Fig. 22, flow reversal (PCB 26-25-24 to PCB 24-25-26)

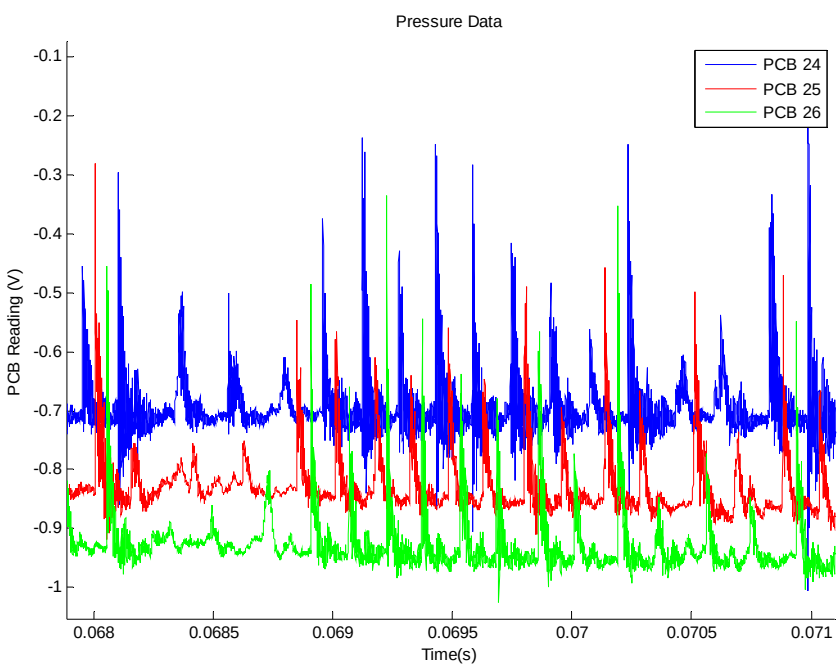

Figure 25. Close up view of Fig. 22, clockwise flow with varying velocities

Since there are regions in Fig. 24Figure **24** where the flow appears to reverse directions, plots of the time between peaks seen by two sequential PCBs versus run time were generated. Figure 26 shows the time the wave front takes to travel between PCBs 24 and 26. A positive time interval indicates a clockwise flow direction while a negative time interval indicates a counter-clockwise flow direction (refer to Fig. 8 for PCB placement). When the time between peaks from the sequential PCBs crosses the zero line, the flow changes direction. Figure 26 illustrates the wave front changing direction multiple times throughout the run. The magnitude of the time between the PCBs is also indicative of the velocity of the wave front. The larger magnitudes indicate a slower velocity and the smaller time differences indicate a higher velocity. Figure 27 is a close up view of Fig. 26 and better illustrates the flow reversal. In Fig. 27, the black line represents the zero line. Figure 28 shows the wave front flow reversal in terms of velocity rather than time. Similar plots for different runs are located in Appendix D. It is interesting to note that both the flow reversal and the velocity changes may also be seen on the high speed video. The reason why the flow reversal occurs is not currently known and further study of this phenomenon will be conducted.

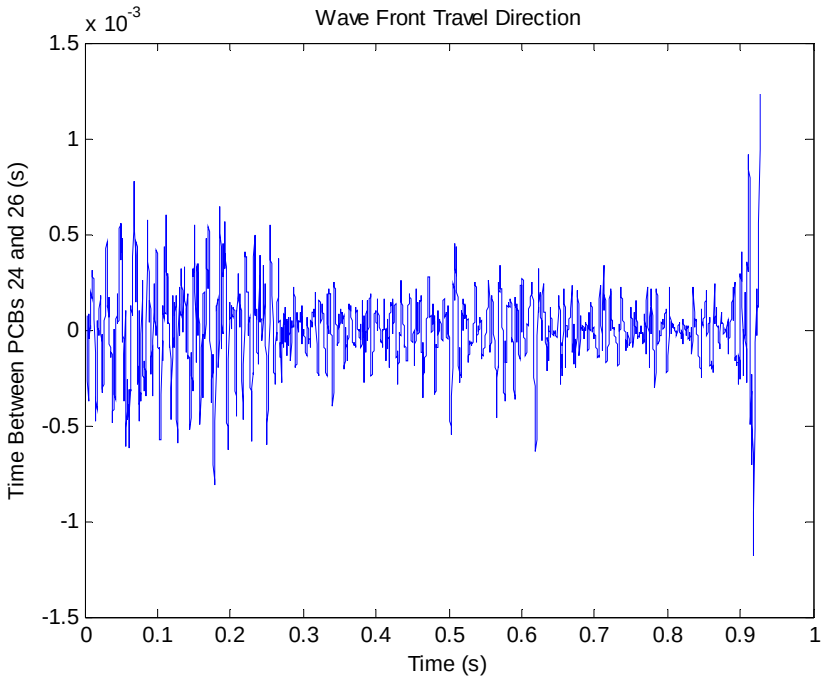

Figure 26. Wave Front Flow Reversal, enriched air, total mass flow rate of 41.1 lbm/min

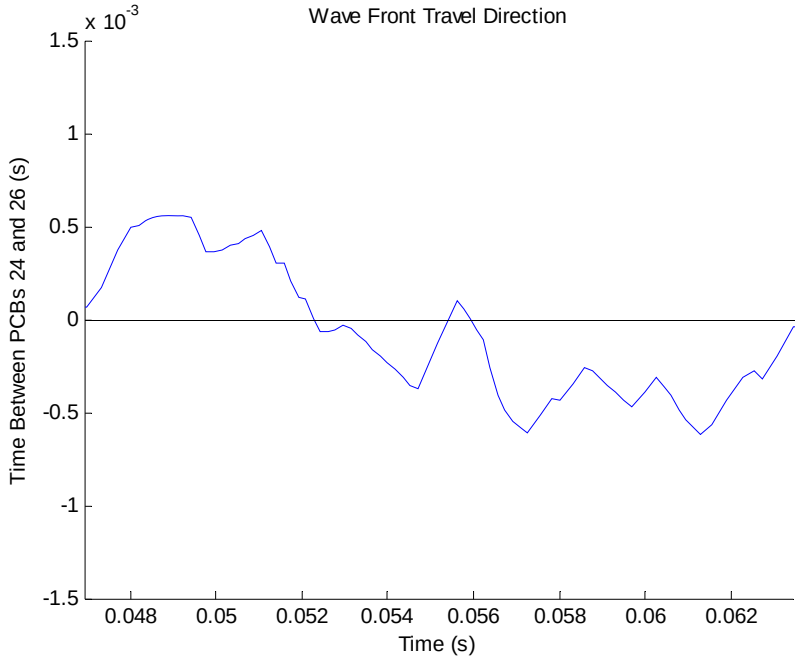

Figure 27. Close up view of Fig. 26

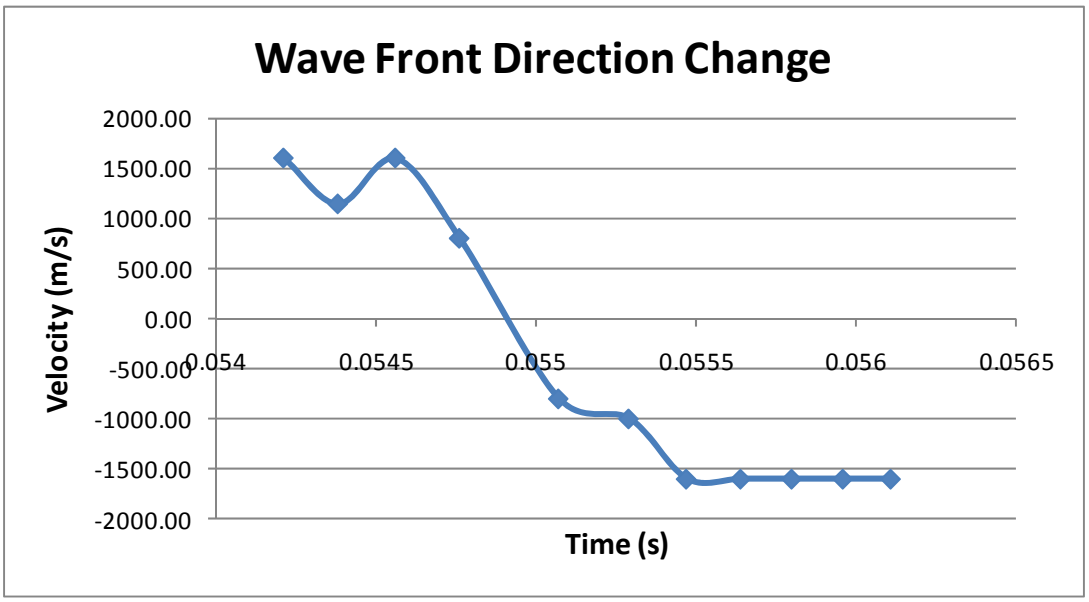

Figure 28. Wave front flow reversal, velocity graph, total mass flow rate of 41.1 lbm/min

To validate the time of flight code, a fast Fourier transform (FFT) of the raw data was compared to a histogram of the velocities calculated by the time of flight code. The FFT yields all the frequencies seen in the pressure data (Fig. 29). The time of flight code was used to generate a histogram of the calculated velocities (Fig. 30). From Figs. 29 and 30, it may clearly be seen that both the time of flight code and the FFT yield similar velocity fields. Both show the primary velocity centered around 1400-1500 m/s and a secondary velocity centered around 600-800 m/s. Both the FFT and the histogram confirm the existence of the secondary, slower velocity seen in Fig. 20Figure **20**.

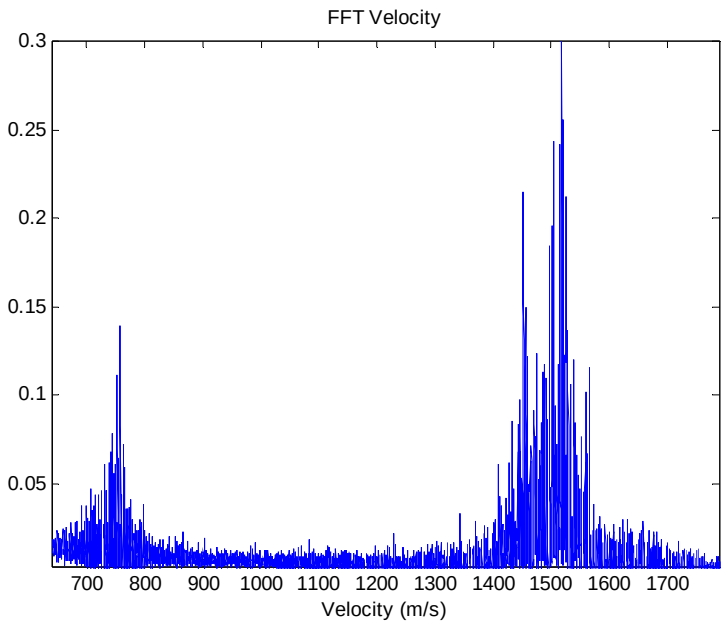

Figure 29. Velocity from fast Fourier transform of pressure data

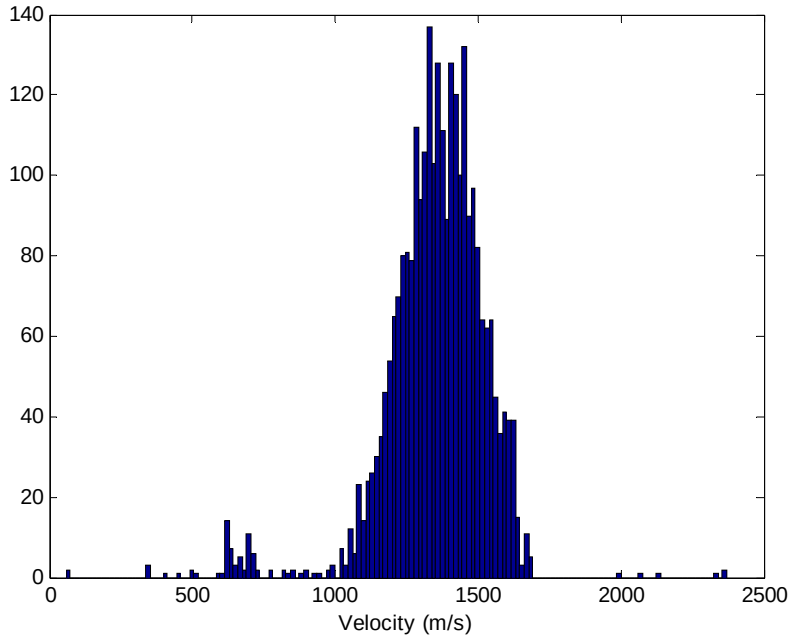

Figure 30. Histogram of velocity from time of flight code

3.8 Error Analysis

The total error is comprised of the bias error (B_x) and the precision error (P_x), as shown in Eq. 6.

$$\boldsymbol{Error} = \sqrt{\boldsymbol{B_x^2} + \boldsymbol{P_x^2}} \tag{6}$$

The bias error comes from the equipment and methods used to take the measurements. Bias errors may result from calibration or data acquisition and reduction. The bias error is calculated using Eq. 7.

$$\boldsymbol{B_x} = \sqrt{\sum_{i=1}^{n} \left[\left(\frac{\partial r}{\partial x_i} \right)^2 \boldsymbol{B_i^2} \right]} \tag{7}$$

In Eq. 7, n is the total number of variables to be examined for a given equation, i represents the variable currently being looked at, B_i is the error associated with the ith component, and $\frac{\partial r}{\partial x_i}$ is the derivative of the equation with respect to the ith component.

The precision error is the result of random factors that influence measurements and may be referred to as the repeatability error. Examination of the data sample for a given confidence interval will yield the precision error. The mean of the data sample ($\bar{X}$) is obtained from Eq. 8.

$$\boldsymbol{\bar{X}} = \frac{\boldsymbol{1}}{\boldsymbol{N}} \sum_{j=1}^{N} \boldsymbol{X_j} \tag{8}$$

In Eq. 8, N is the total number of data points in the sample and j represents the data point being examined. The standard deviation of the sample (S_x) is found from Eq. 9.

$$\boldsymbol{S_x} = \sqrt{\frac{\boldsymbol{1}}{\boldsymbol{N-1}}\sum_{\boldsymbol{j=1}}^{\boldsymbol{N}}\left(\boldsymbol{X_j} - \bar{\boldsymbol{X}}\right)^{\boldsymbol{2}}} \tag{9}$$

The confidence interval represents a range in which the mean of an infinite population would lie. For this work, a 95% confidence interval was chosen. This means that there is a 95% certainty that the mean of the infinite population would lie within the bounds of the uncertainty interval ($\bar{X} \pm P_x$). If an infinite number of measurements were obtained, a Gaussian distribution would result. However, since the data sets are not infinite, it is necessary to use a t-distribution to determine the precision error, as shown in Eq. 10.

$$\boldsymbol{P_x} = \frac{\boldsymbol{tS_x}}{\sqrt{\boldsymbol{N}}} \tag{10}$$

In Eq. 10, t is taken to be 2 for a 95% confidence interval of a data set with greater than 30 data points (13; 15)

Using the above equations, the uncertainties in the total mass flow rates, air mass flow rates, fuel mass flow rates, equivalence ratios, and detonation velocities were calculated. The average uncertainty for the total mass flow rate was 2.57% with a maximum uncertainty of 3.57%. The average uncertainty for the air mass flow rate was 2.66% with a maximum uncertainty of 3.75%. The average uncertainty for the fuel mass

flow rate was 4.52% with a maximum uncertainty of 6.56%. The average uncertainty for the equivalence ratio was 0.158% with a maximum uncertainty of 0.210%. The average uncertainty for the detonation velocity was 36.1% with a maximum uncertainty of 68.1%. The full uncertainties for these values are tabulated in Appendix E.

IV. RESULTS AND DISCUSSION

4.1 Overview

This research included an investigation of the parameter space in which the RDE produced a detonation. Due to the simplicity of the RDE, the primary parameters examined were the mass flow rate and equivalence ratios. Velocity profiles were also used to validate the success of the run. From previous work (10; 11), the detonation velocity for RDEs running on hydrogen air were expected to be approximately 1400 m/s.

Both standard compressed air (approximately 21% oxygen) and enriched tuber air (approximately 23% oxygen) were used in these tests. A large portion of the runs were devoted to standard air since the ultimate goal is to use standard air as the oxidizer. In the original testing, standard air runs were unsuccessful, so enriched air was used to begin mapping the parameter space. Near the end of the test period, some successes (i.e. repeatable, full-length runs) were achieved with standard air; those successes are reported later.

4.2 Parameter Space, Enriched Air

Figure 31 contains all successful points, i.e. those for which both criteria were met, and thus represents the enriched air parameter space for the RDE. The maximum detonation velocity was 1420 m/s, the minimum was 1207 m/s, and the average was 1301 m/s.

Examination of Fig. 31Figure **31** reveals what appears to be a linear lower bound for the parameter space. If the trend line were extended further, it would include two

points of lower mass flow rates and higher equivalence ratios that were omitted since repeatability was not confirmed.

Figure 31 shows equivalence ratio sweeps for total mass flow rates arbitrarily chosen to be approximately 40, 45, and 50 lbm/min. The first successful run was obtained for a total mass flow rate of approximately 50 lbm/min. From there, tests were conducted with lower total mass flow rates in an attempt to determine the minimum total mass flow rate necessary for successful detonation.

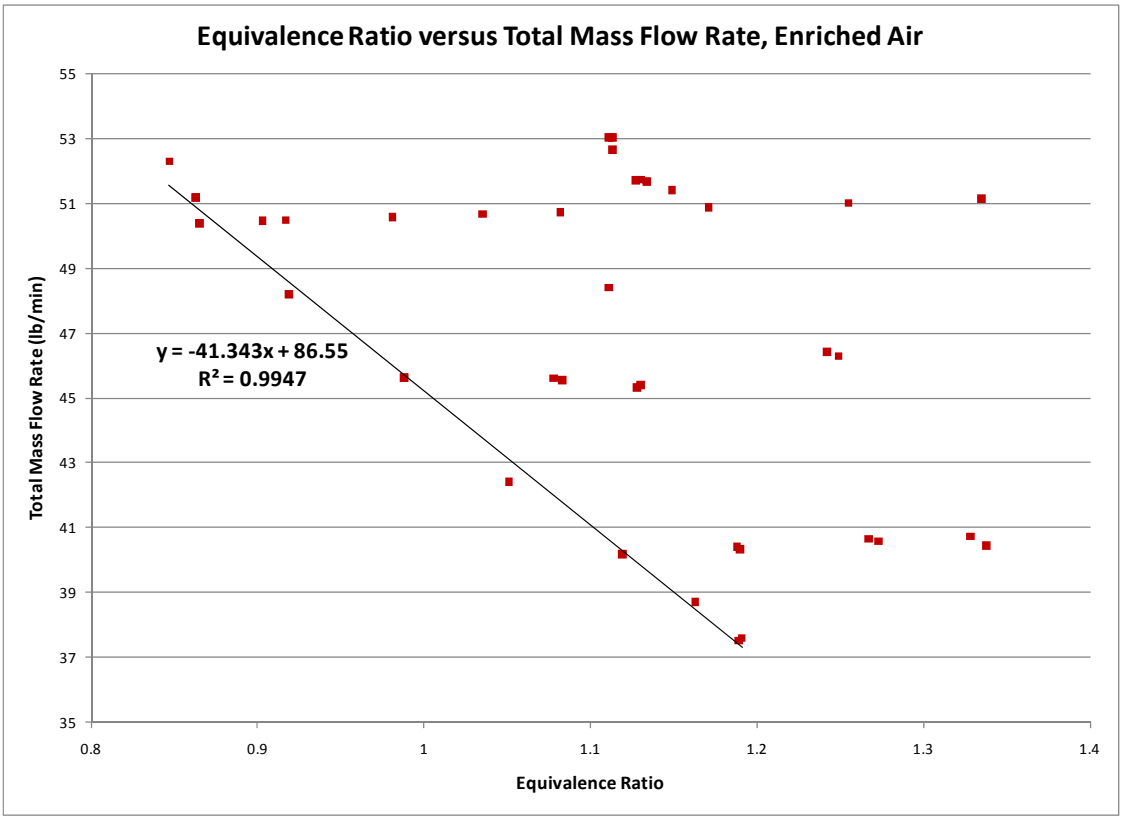

Figure 31. Parameter space with linear lower boundary line

In order to determine any commonalities among the points along the lower left hand boundary in Fig. 31, the parameter space was mapped as a function of equivalence ratio and fuel mass flow rate, as shown below in Fig. 32Figure **32**. This figure clearly shows that the fuel mass flow rate for enriched air needs to be larger than 1.4 lbm/min for the RDE to run. The relationship between the fuel flow rate and other parameters is not understood at this time. More work should be conducted to determine how the fuel flow rate correlates with other parameters.

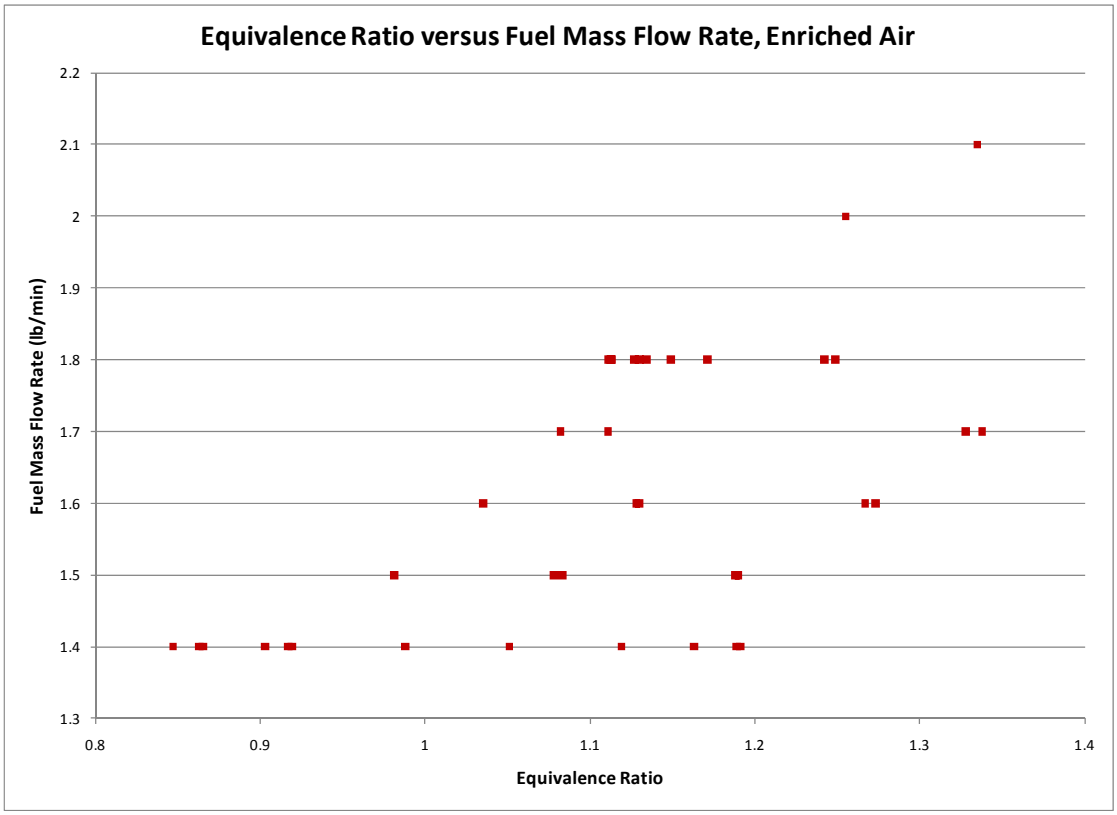

Figure 32. Parameter space for enriched air based on fuel mass flow rate

Figure 33 shows the parameter space as a function of air mass flow rate and fuel mass flow rate. Again, the figure shows that for the RDE to produce a detonation, a minimum fuel flow rate of 1.4 lbm/min is necessary. Figure 33 also shows an upper boundary above which fuel flow rates will not produce a detonation.

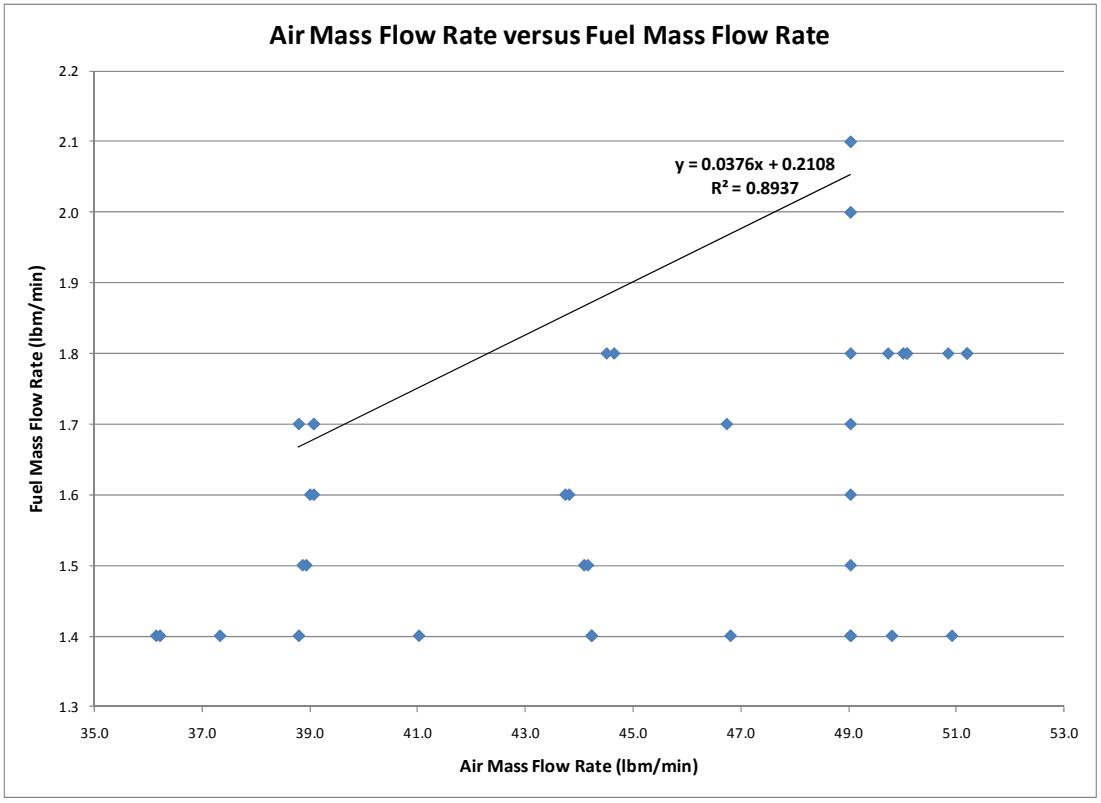

Figure 33. Parameter space for enriched air based on air and fuel mass flow rates

4.3 Standard Air

Based upon the observation that the RDE needs a minimum fuel flow rate of 1.4 lbm/min (see Fig. 32) to produce a detonation using enriched air, the standard air runs were reevaluated using Figs. 34 and 35. A plot of equivalence ratio and fuel mass flow

rate was generated (Fig. 34) which included the successful enriched air runs and the standard air runs which stayed in the channel for the duration of the run but were not repeatable. Figure 34 shows that these partially successful standard air runs were primarily conducted with fuel flow rates less than 1.4 lbm/min due to maintaining an equivalence ratio of approximately one and a total mass flow rate between approximately 20 and 35 lbm/min.

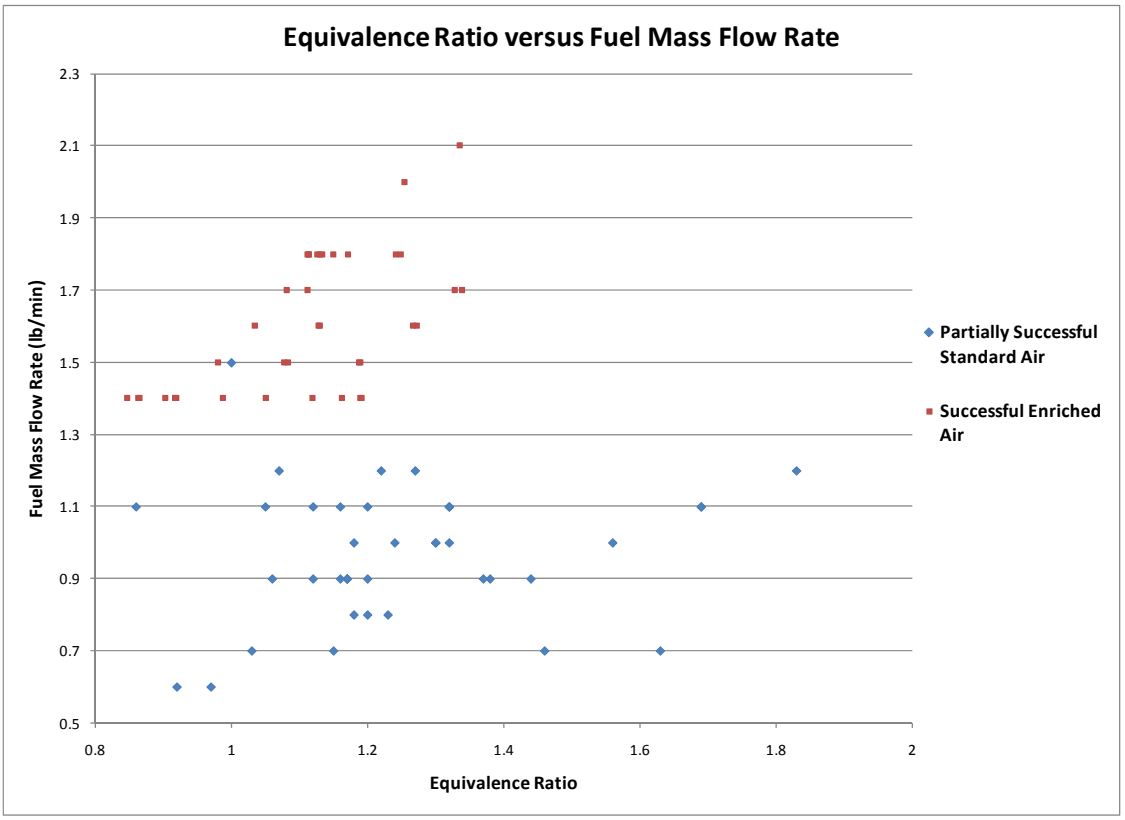

Figure 34. Equivalence ratio and fuel mass flow rate for successful enriched air and partially successful standard air runs

Another plot (Fig. 35Figure **35**) of the successful enriched air runs and the partially successful standard air runs (runs which stayed in the channel for the duration of the run)

was created for equivalence ratio and total mass flow rate. Figure 35 shows that the standard air runs were primarily conducted with total mass flow rates of less than 35 lbm/min.

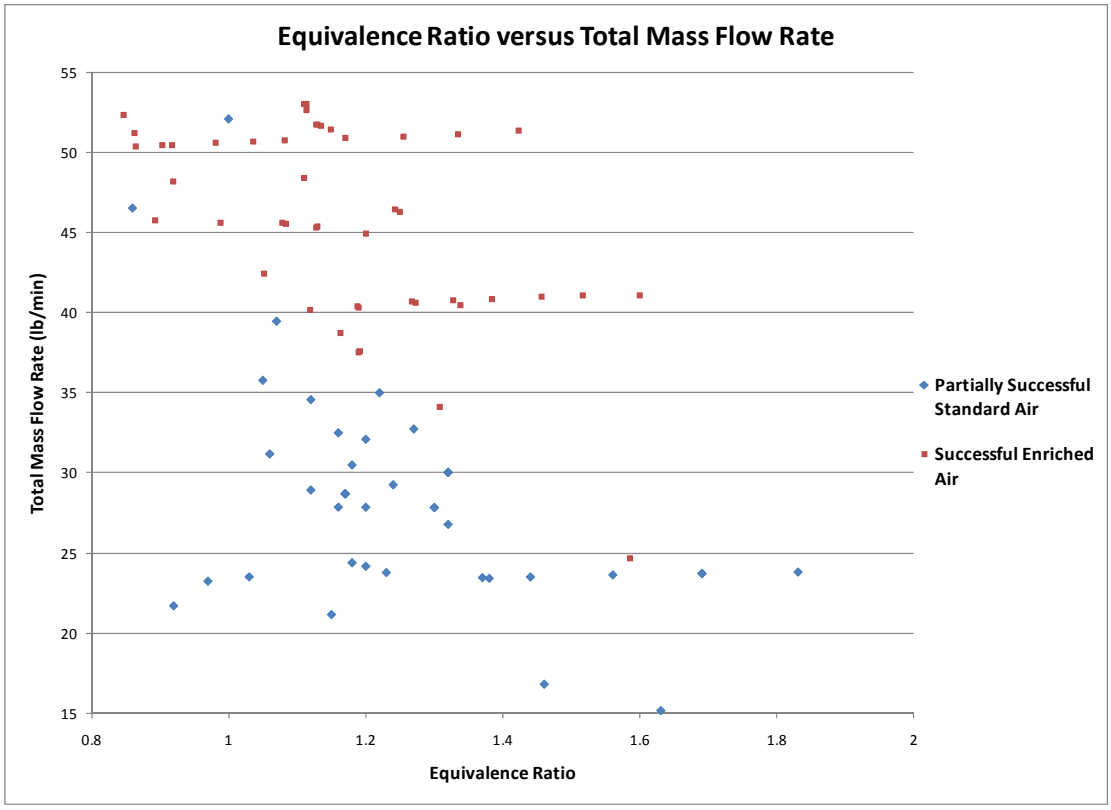

Figure 35. Equivalence ratio and total mass flow rate for enriched air and partially successful standard air runs

From these observations, it was hypothesized that a standard air run conducted for a total mass flow rate of 35 lbm/min or less with a minimum fuel flow rate of 1.4 lbm/min would yield a successful, repeatable detonation. To test this hypothesis, additional standard air runs were conducted. The fuel flow rates, total mass flow rates, air flow rates, equivalence ratios, and velocities are summarized in Table 2. Row 1 (fuel

flow rate of 1.3 lbm/min) was unsuccessful. Rows 2 and 3 (fuel flow rates of 1.4 and 1.5 lbm/min) were successful.

Table 2. Standard air run conditions and results

Fuel Mass Flow Rate (lbm/min)	Total Mass Flow Rate (lbm/min)	Air Mass Flow Rate (lbm/min)	Equivalence Ratio	Velocity (m/s)
1.3	30.5	29.2	1.55	N/A
1.4	30.5	29.1	1.63	1330
1.5	30.5	29.0	1.75	1410

Both the 1.4 and 1.5 lbm/min fuel flow rate cases were successfully repeated three times. In order to test the theory that a fuel flow rate of at least 1.4 lbm/min is necessary, runs were attempted fuel flow rates of 1.3 lbm/min. The runs conducted at this condition were not repeatable. Figure 36 shows the enriched air parameter space with the two successful standard air runs. Appendix F contains graphs of the full test space, including failed runs.

High speed data from the PCBs was not available for these runs, so the high speed video was used to verify the success of the runs. From the number of frames the detonation wave took to complete one revolution, approximate run velocities were calculated. The velocities correspond well with the run velocities seen for the successful enriched air runs. When high speed data is available, these runs will be repeated for additional verification.

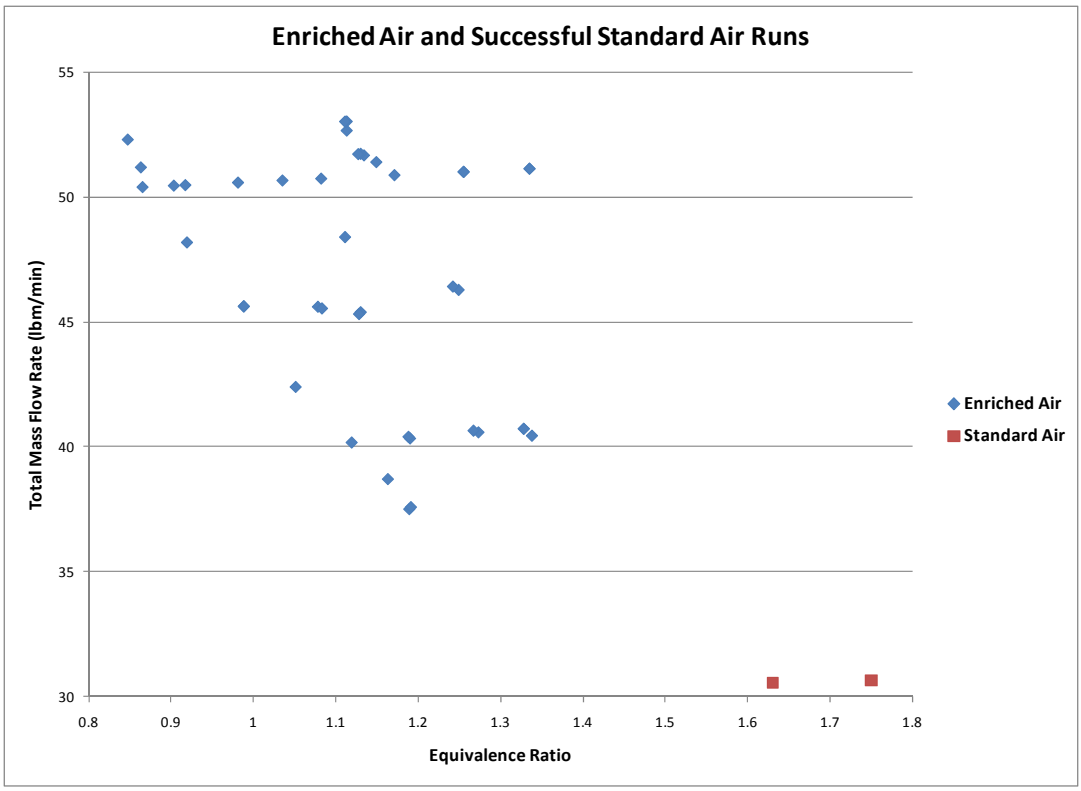

Figure 36. Parameter space for enriched air runs with successful standard air runs

4.3 Velocity, Enriched Air

The other primary area of interest is the detonation velocity. The CJ velocity for hydrogen-standard air is 1950 m/s. However, previous researchers (10; 11) have found that the detonation velocities seen in RDEs tend to be lower, on the order or 1400 m/s. Possible explanations for this include the fresh propellants interacting with the detonation products to create a non-reacting zone and non-ideal mixing of the propellants due to the short time between subsequent detonation waves (16). For the runs with enriched air, the detonation velocities varied from 1200 m/s to 1420 m/s. Figures 37-39 show the velocity and equivalence ratios for three different regions of total mass flow rates for the runs conducted using enriched air. These three regions correspond to the three total mass flow

rates for which equivalence ratio sweeps were performed (see Fig. 31Figure **31**). The points are labeled by their fuel mass flow rate (in lbm/min) rather than their total mass flow rate to show that as the fuel mass flow rate increases, the detonation velocity increases. No such trend was observable when the points were labeled by their total mass flow rate.

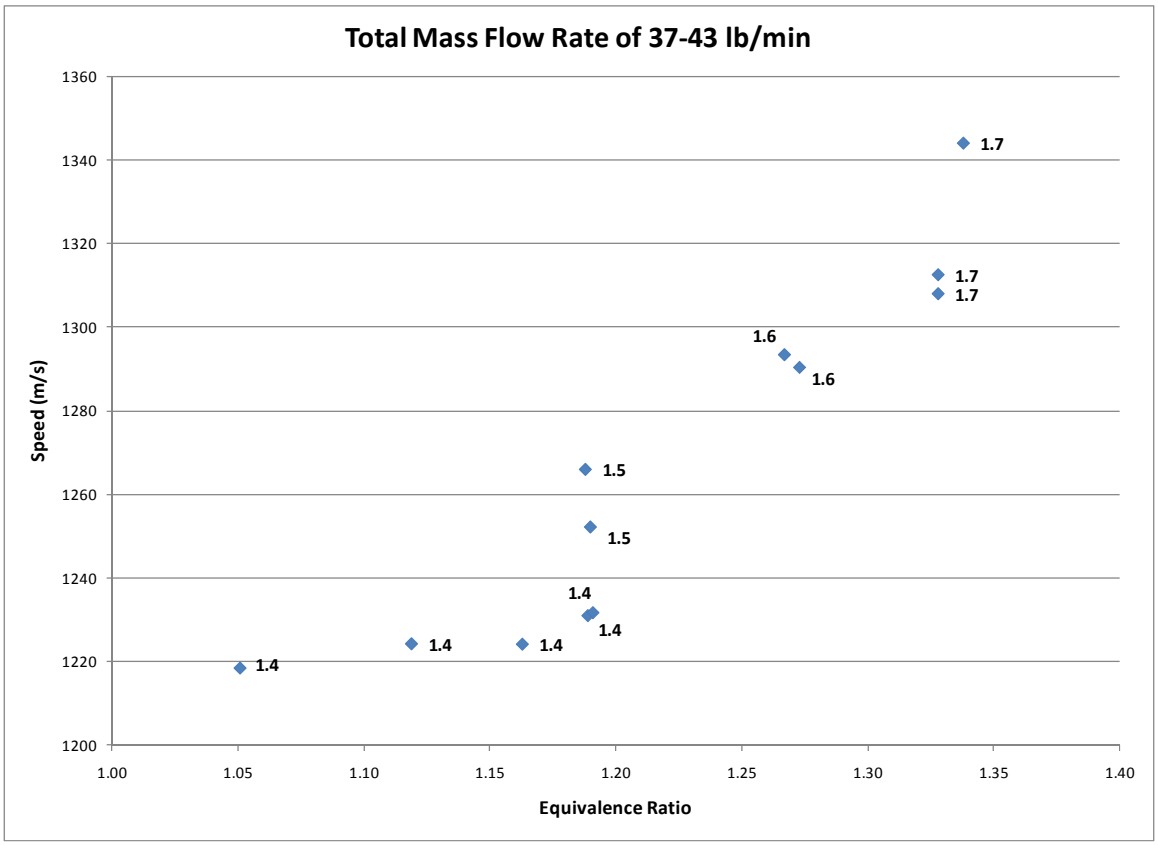

Figure 37. Speed and equivalence ratio for total mass flow rates of 37-43 lbm/min

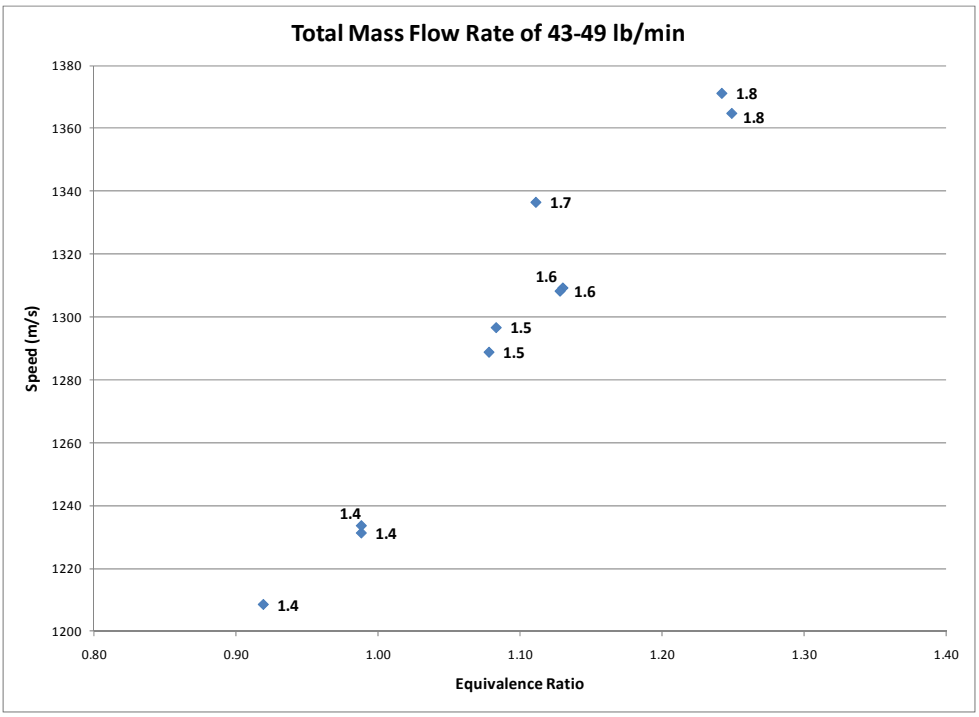

Figure 38. Speed and equivalence ratio for total mass flow rates of 43-49 lbm/min

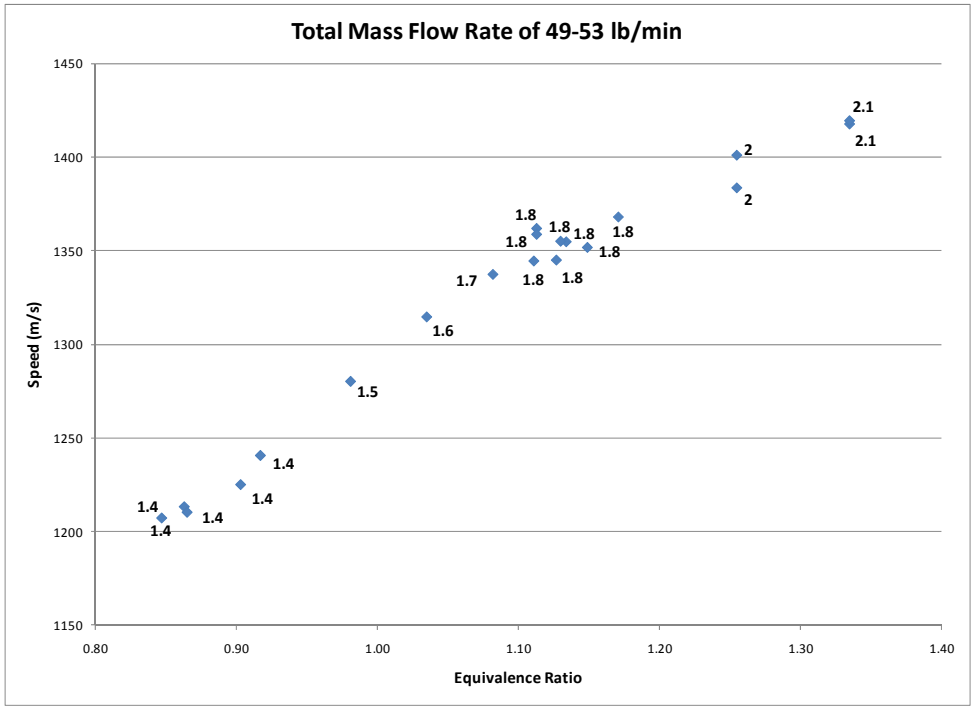

Figure 39. Speed and equivalence ratio for total mass flow rates of 49-53 lbm/min

For the enriched air runs, Fig. 40Figure **40** was generated with all the runs delineated by their respective fuel mass flow rates. From this graph, there appears to be a linear left hand boundary indicating that for a given fuel flow rate there is a minimum equivalence ratio which will yield a successful run. More runs need to be conducted to confirm this.

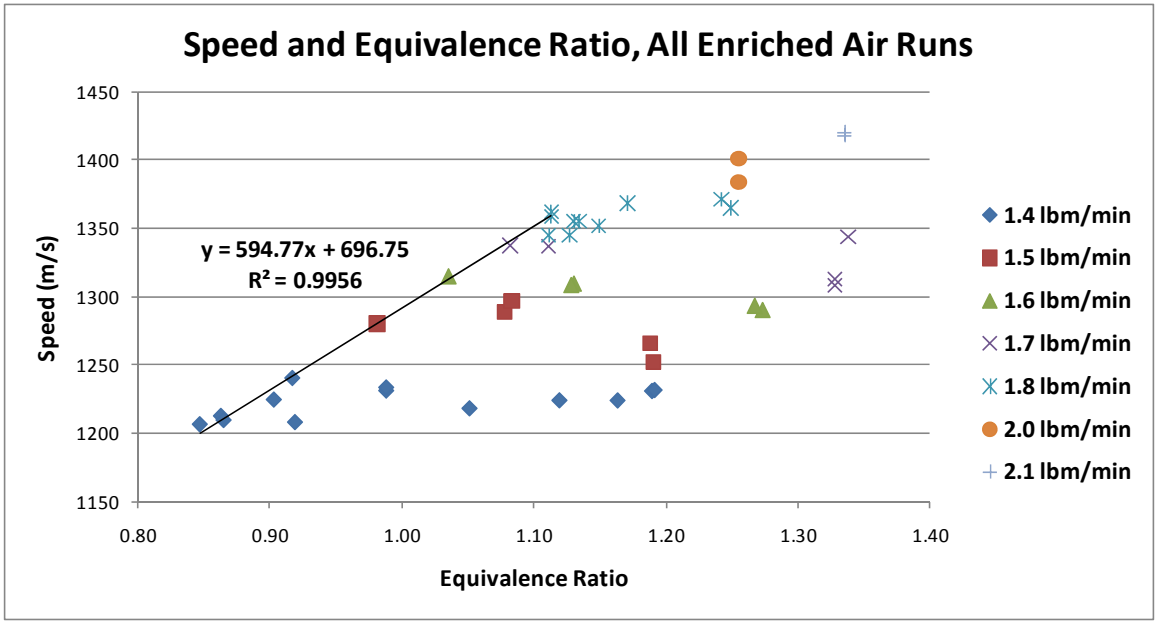

Figure 40. Speed and equivalence ratio for all successful enriched air runs

V. CONCLUSIONS AND RECOMMENDATIONS

5.1 Conclusions

The goal of this research was to determine operational mass flow rates and equivalence ratios for the RDE using enriched and standard air. A lower left hand boundary was found for enriched air. This boundary corresponds to a fuel mass flow rate of 1.4 lbm/min. For the enriched air runs, a correlation between the fuel mass flow rate and the detonation velocity was also observed. As the fuel mass flow rate increases, the detonation velocity also increases.

Runs using standard air were also attempted. However, although several of these tests remained in the annulus for the full run time, none of these original tests were repeatable. Upon analysis of the run parameters, it was noted that only one of the full runs had a fuel mass flow rate greater than 1.4 lbm/min. Many of the runs that did not remain in the channel for the full length of the run had fuel mass flow rates greater than 1.4 lbm/min but all of them had high total mass flow rates. The runs that remained in the channel for the desired length of time primarily had much lower total mass flow rates. It is therefore hypothesized that the total mass flow rate determines whether or not the combustion will remain in the channel and that the fuel mass flow rate influences the success and repeatability of the run. Lower total mass flow rates appear to remain in the annulus for the full run while higher total mass flow rates did not. The higher fuel mass flow rates (higher equivalence ratios) potentially help with propellant mixing in the channel. The fuel mass flow rates used in early runs were likely not high enough to

promote mixing. From these observations, two additional tests were conducted for a total mass flow rate of approximately 30.5 lbm/min and fuel flow rates of 1.4 lbm/min and 1.5 lbm/min (equivalence ratios of 1.63 and 1.76). These tests met the criteria for a successful run.

The results from both the standard and enriched air runs indicate that the success or failure of a run is the result of how well the propellants mix. Lower fuel flow rates were unsuccessful for both regular and enriched air runs. For enriched air it was also observed that as the total mass flow rate increases for a given fuel flow rate (lower equivalence ratio) the run velocity decreases. This could result from higher air flow rates contributing to decreased mixing. The lack of successful standard and enriched air runs for fuel flow rates less than 1.4 lbm/min also appears to indicate that a minimum fuel injection rate is necessary to promote mixing.

Additionally, it is noted that operating at lower total mass flow rates and higher fuel flow rates results in higher equivalence ratios (1.63 and 1.76 for the additional standard air runs runs, for example). These higher equivalence ratios do not necessarily reflect the actual equivalence ratios seen by the detonation front. Poorly mixed propellants would result in lower equivalence ratios more in line with traditional detonation theory.

By meeting the research objectives, two of the three historical challenges were addressed; the engine was successfully run on hydrogen-air and steady detonation wave propagation upon initiation was achieved. Research still needs to be conducted on the third historical challenge, the pressure loss across the inlet.

5.2 Recommendations

This work has shown that detonations may be obtained with standard air for the current geometry under certain conditions. Future work should initially focus on total mass flow rates of less than 35 lbm/min with minimum fuel mass flow rates of 1.4 lbm/min. Additional tests should be done to determine if higher total mass flow rates will successfully generate a detonation.

Visualization of the propellant mixing at the inlet to the combustion chamber would be beneficial in order to better understand how the propellants interact under various conditions. This would also allow insight into the local equivalence ratio seen by the detonation front.

Finally, new injection schemes should be created to determine the best way to promote mixing of the propellants.

APPENDIX A. ONE-DIMENSIONAL DETONATION WAVE CHARACTERISTICS

Most attempts to explain detonation waves have utilized a one-dimensional model. The detonation wave shown in Fig. 41 is stationary with the reactants flowing into and the products flowing away from the detonation wave.

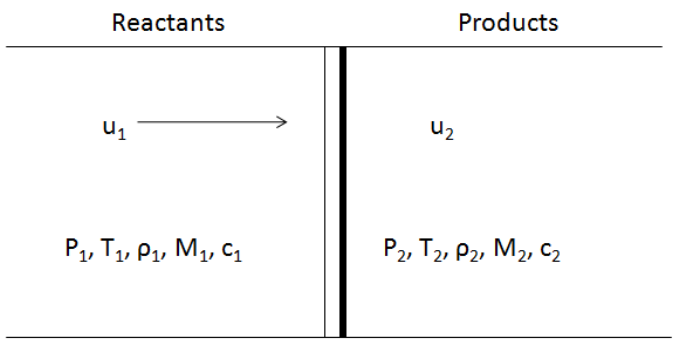

Figure 41. One-Dimensional model of a detonation wave

The Hugoniot equation relates pressure and volume for any compressible gas. This P-*v* relationship describes all of the available equilibrium states. Since the system undergoes a detonation, which can be modeled as an instantaneous change from one state to another (or a shock), a Rayleigh line may be drawn on the Hugoniot curve that accounts for heat addition and connects the initial and final states of the system. Figure 42 illustrates the relationship between the Rayleigh line and the Hugoniot curve (17).

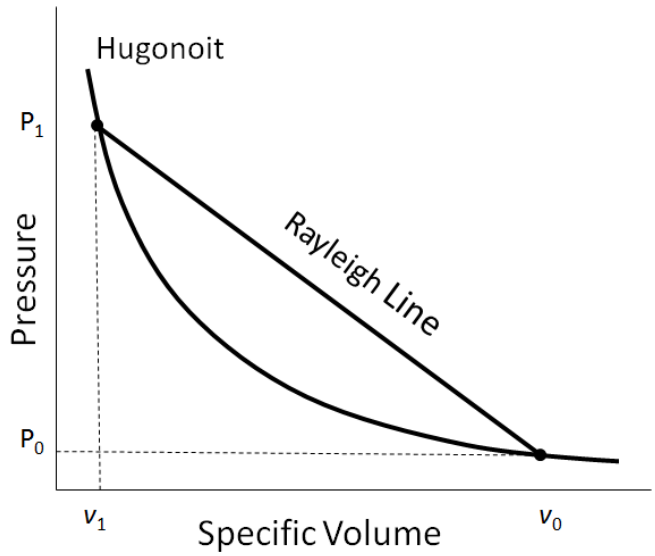

Figure 42. P-v Hugoniot curve with Rayleigh line

To derive the Rayleigh line and the Hugoniot curve using a one-dimensional analysis, it is assumed that the flow is steady, the area is constant, the gas is ideal with constant and equal specific heats, there are no body forces, and the system is adiabatic. The following equations for conservation of mass, momentum, and energy are used.

$$\boldsymbol{\rho_1 u_1 = \rho_2 u_2} \tag{11}$$

$$\boldsymbol{P_1 + \rho_1 u_1^2 = P_2 + \rho_2 u_2^2} \tag{12}$$

$$\boldsymbol{h_1 + \frac{1}{2} u_1^2 = h_2 + \frac{1}{2} u_2^2} \tag{13}$$

In Eqs. 11 through 13, ρ is the density of the gas, u is the velocity, P is the pressure, and h is the specific enthalpy. The subscripts refer to the state of the system before and after the shock, respectively, as shown in Fig. 41Figure **41**. The Rayleigh line is found from

the simultaneous solution of the mass and momentum equations (Eqs. 11 and 12). The equations may be solved for either u_1 or u_2.

$$\boldsymbol{u_1^2 = \frac{1}{\rho_1^2}\left[\frac{P_2 - P_1}{1/\rho_1 - 1/\rho_2}\right]} \tag{14}$$

$$\boldsymbol{u_2^2 = \frac{1}{\rho_2^2}\left[\frac{P_2 - P_1}{1/\rho_1 - 1/\rho_2}\right]} \tag{15}$$

To obtain the Hugoniot curve, Eqs. 13, 14, and 15 are combined with the following ideal gas relations (Eqs. 16 through 18) and the caloric equation of state (Eq. 19):

$$\boldsymbol{P = \rho R T} \tag{16}$$

$$\boldsymbol{\gamma = \frac{C_p}{C_v}} \tag{17}$$

$$\boldsymbol{R = C_p - C_v} \tag{18}$$

$$\boldsymbol{h(T) = \sum Y_i h_{f,i}^{\circ} + C_p\left(T - T_{ref}\right)} \tag{19}$$

In Eqs. 16-19, R is the specific gas constant, γ is the ratio of specific heats, C_p is the specific heat at constant pressure, C_v is the specific heat at constant volume, Y_i is the mass fraction of species *i*, $h_{f,i}^{\circ}$ is the enthalpy of formation of species *i*, T is the temperature of the species, and T_{ref} is the reference temperature (298 K). After combining these equations, the Hugoniot curve (sometimes referred to as the Rankine-Hugoniot curve) is (5)

$$\boldsymbol{\frac{\gamma}{\gamma - 1}\left[\frac{P_2}{\rho_2} - \frac{P_1}{\rho_1}\right] - \frac{1}{2}(P_2 - P_1)\left(\frac{1}{\rho_2} + \frac{1}{\rho_1}\right) - q = 0} \tag{20}$$

Note that in Eq. 20, q is the heat released by the system.

Hugoniot curves with Rayleigh lines as shown in Fig. 42Figure **42** may be drawn for the reactants of a system as well as the products of the system. A Hugoniot curve for the products of a system has its origin at the point that coincides with the initial pressure, P_1, and the initial volume, v_1. Since this Hugoniot curve includes all the available states in which the reaction products may be found, the origin of the curve lies below the actual curve. Figure 43 shows the Rankine-Hugoniot curve, with point A as the origin of the curve.

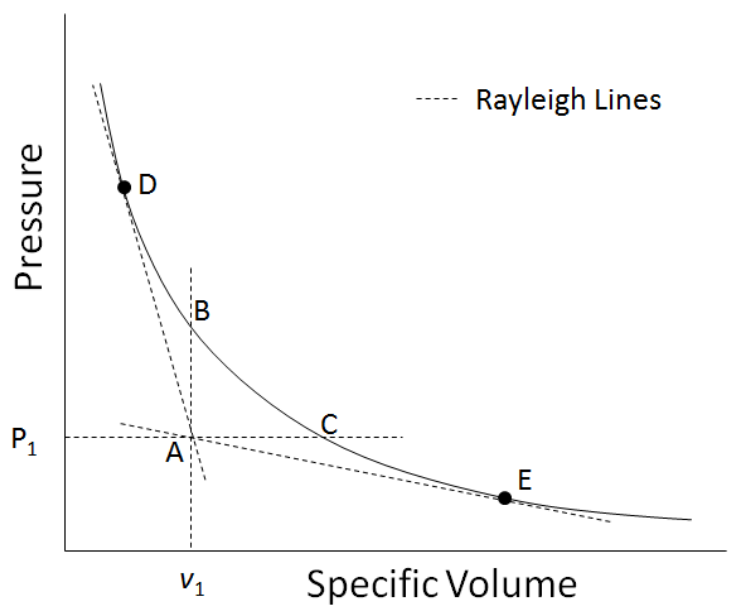

Figure 43. Rankine-Hugoniot curve

As shown in Fig. 43Figure **43**, there are two potential end states for the reaction products. The first, designated by point D, is the case in which P_2 is greater than P_1 and therefore is indicative of a detonation reaction. The second end state, designated by point E, is the

case in which P_2 is less than P_1 and is therefore indicative of a deflagration reaction. Since there are two possible end states for the reaction, there are two limiting Rayleigh lines, as shown in Fig. 43Figure **43**. These two limiting Rayleigh lines are each tangent to the Hugoniot curve, and the points of tangency are designated Chapman-Jouguet points. The final two lines shown in Fig. 43Figure **43** show the initial states of the system (on A-B and A-C in Fig. 43Figure **43**) which are bounds for the regions of physically possible states. States which lie between points C and E are associated with weak deflagrations, while states that lie below point E are associated with strong deflagrations. Similarly, states which are between points B and D are associated with weak detonations while states that lie above point D are associated with strong detonations (5). The Chapman-Jouguet points, points D and E in Fig. 43Figure **43**, are considered the steady-state detonation and deflagration conditions, respectively (5).

Table A 1. Hugoniot curve region classifications

Section of Hugoniot Curve	Characteristic	Unburned Gas Velocity	Burned Gas Velocity
Above D	Strong Detonation	Supersonic	Subsonic
D-B	Weak Detonation	Supersonic	Supersonic
B-C	Inaccessible	N/A	N/A
C-E	Weak Deflagration	Subsonic	Subsonic
Below E	Strong Deflagration	Subsonic	Supersonic

Considering just the upper Rayleigh line in Fig. 43, if the magnitude of the slope of this Rayleigh line is greater than the slope of the limiting Rayleigh line, then the wave

speed is greater than the steady-state detonation wave speed. As Fig. 44Figure **44** clearly shows, this condition indicates that there will be two potential states for the products. One of the final states will lie above the Chapman-Jouguet point in the strong detonation region while the other will lie below in the weak detonation region. Both strong and weak detonations are difficult to obtain and sustain. Therefore, if such a condition is created, the system will transition back to the upper Chapman-Jouguet point (D) in order to sustain a steady-state detonation (1; 17; 5).

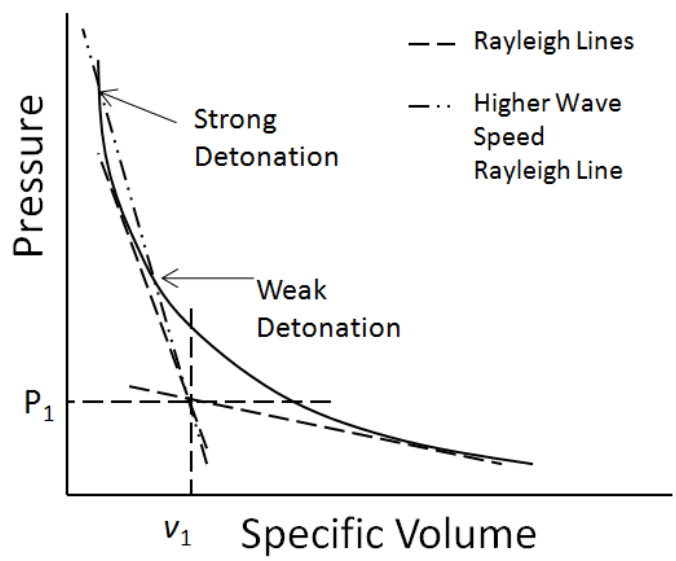

Figure 44. Rankine-Hugoniot curve with a Rayleigh line for higher wave speeds

In addition to the Rankine-Hugoniot curve, a one-dimensional analysis may be used to determine the detonation wave profile. In the 1940s, Zeldovich, von Neumann, and Döring (5) independently determined the structure of a detonation wave based upon a

one-dimensional analysis, shown in Fig. 45Figure **45**. In Fig. 45Figure **45**, the direction the detonation wave is propagating is indicated by the arrow labeled V_D.

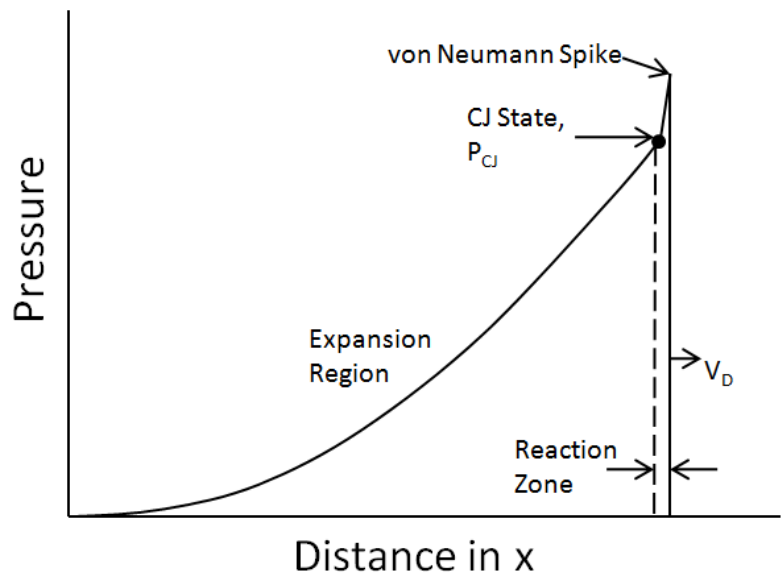

Figure 45. Zeldovich, von Neumann, and Döring detonation wave profile

This model, known as the ZND model, consists of a shock coupled with a thin flame front followed by a region of expansion. The shock initiates the combustion of the gases and the flame front provides heat addition. For a steady-state detonation, the shock and flame front propagate at a detonation velocity that coincides with the Chapman-Jouguet point. The region between the shock and the flame front is characterized by its high pressure, P_S, and is known as the von Neumann spike. Once heat is added to this high pressure region via the flame front, the temperature of the reaction increases and the pressure decreases. After passage of the flame front, the burned gases are in their final state (equivalent to point D in Fig. 43Figure **43**). The pressure at this final state, P_2, is much lower than the pressure in the von Neumann spike; however, this pressure is still

significantly higher than the initial pressure. For a detonation occurring in a closed tube or channel, the burned gases then undergo an expansion such that the pressure away from the detonation wave (P_3) is much lower than the pressure (P_2) just behind the detonation wave (1).

APPENDIX B. SENSITIVITY ANALYSIS DATA

Table B 1. Case 1 Sensitivity Analysis Data

Standard Deviations Above Mean	Consecutive Points Above Mean	Hold Time (microsec)	Average Run Velocity (m/s)
0	1	60	2818.50
0	1	80	2352.20
0	1	100	1665.90
0	1	120	1492.00
0	2	60	2562.10
0	2	80	2108.30
0	2	100	1584.40
0	2	120	1456.60
0	3	60	2269.40
0	3	80	1888.10
0	3	100	1521.10
0	3	120	1425.80
0	4	60	2063.30
0	4	80	1758.70
0	4	100	1486.10
0	4	120	1407.90
1	1	60	1360.30
1	1	80	1352.90
1	1	100	1349.60
1	1	120	1348.70
1	2	60	1352.80
1	2	80	1348.10
1	2	100	1346.70
1	2	120	1346.00
1	3	60	1341.00
1	3	80	1339.80
1	3	100	1339.40
1	3	120	1339.20
1	4	60	1325.40
1	4	80	1325.40
1	4	100	1325.00
1	4	120	1324.80
2	1	60	1282.20
2	1	80	1281.70
2	1	100	1281.70
2	1	120	1281.70
2	2	60	1241.70
2	2	80	1241.70
2	2	100	1241.70
2	2	120	1241.70
2	3	60	1148.50
2	3	80	1148.50
2	3	100	1148.50
2	3	120	1148.50
2	4	60	1013.50
2	4	80	1013.50
2	4	100	1013.50
2	4	120	1013.50

Table B 2. Case 2 Sensitivity Analysis Data

Standard Deviations Above Mean	Consecutive Points Above Mean	Hold Time (microsec)	Average Run Velocity (m/s)
0	1	60	2818.50
0	1	80	2352.20
0	1	100	1665.90
0	1	120	1492.00
0	2	60	2562.10
0	2	80	2108.30
0	2	100	1584.40
0	2	120	1456.60
0	3	60	2269.40
0	3	80	1888.10
0	3	100	1521.10
0	3	120	1425.80
0	4	60	2063.30
0	4	80	1758.70
0	4	100	1486.10
0	4	120	1407.90
1	1	60	1360.30
1	1	80	1352.90
1	1	100	1349.60
1	1	120	1348.70
1	2	60	1352.80
1	2	80	1348.10
1	2	100	1346.70
1	2	120	1346.00
1	3	60	1341.00
1	3	80	1339.80
1	3	100	1339.40
1	3	120	1339.20
1	4	60	1325.40
1	4	80	1325.40
1	4	100	1325.00
1	4	120	1324.80
2	1	60	1282.20
2	1	80	1281.70
2	1	100	1281.70
2	1	120	1281.70
2	2	60	1241.70
2	2	80	1241.70
2	2	100	1241.70
2	2	120	1241.70
2	3	60	1148.50
2	3	80	1148.50
2	3	100	1148.50
2	3	120	1148.50
2	4	60	1013.50
2	4	80	1013.50
2	4	100	1013.50
2	4	120	1013.50

APPENDIX C. TIME OF FLIGHT CODE VELOCITY GRAPHS

Enriched Air

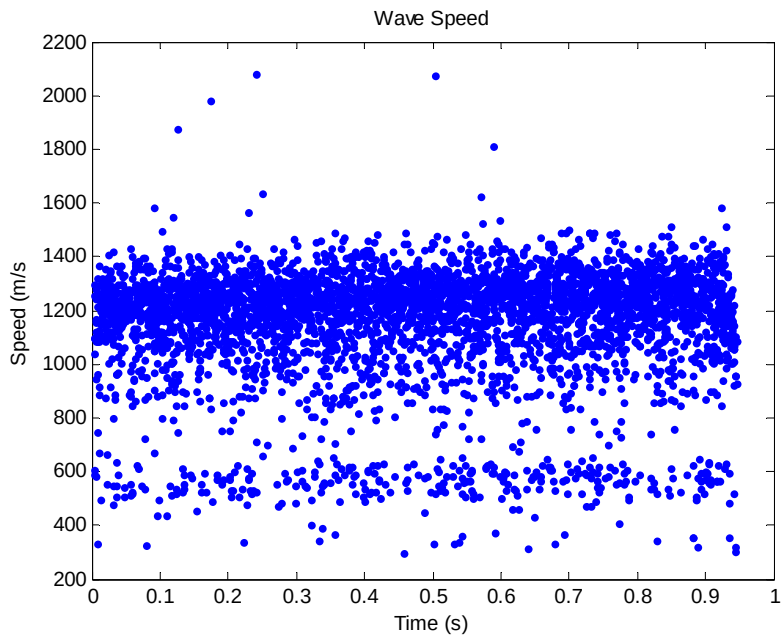

Figure 46. Wave speed data sample 1 φ=0.87, $\dot{m}_{tot}$=50.39 lbm/min, $\dot{m}_f$=1.4 lbm/min

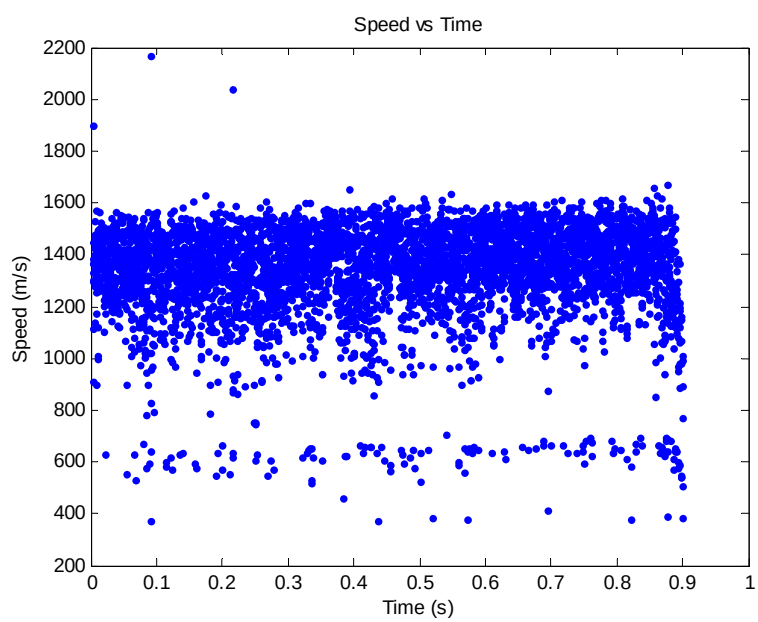

Figure 47. Wave speed data sample 2 φ=1.13, $\dot{m}_{tot}$=51.72 lbm/min, $\dot{m}_f$=1.8 lbm/min

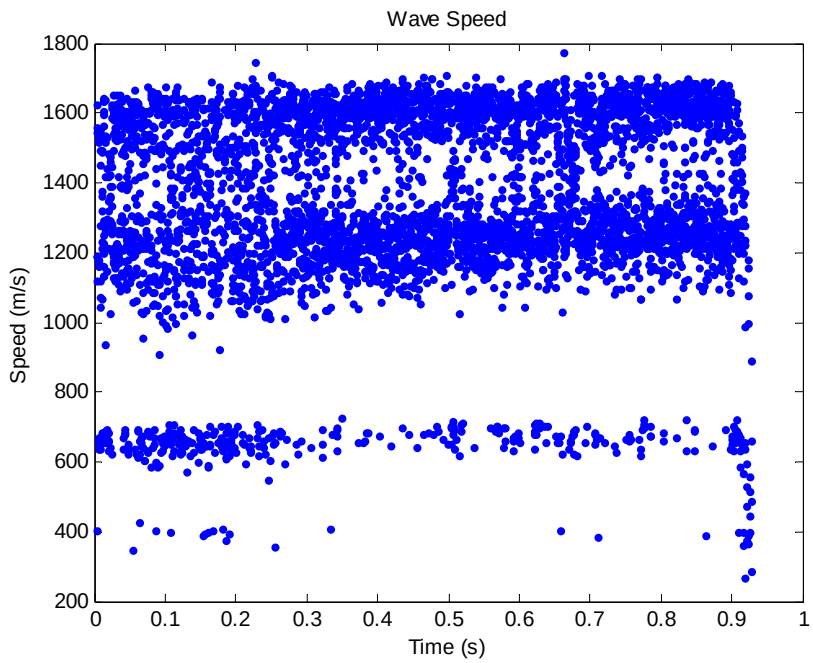

Figure 48. Wave speed data sample 3 φ=1.6, $\dot{m}_{tot}$=41.1 lbm/min, $\dot{m}_f$=2 lbm/min

Regular Air

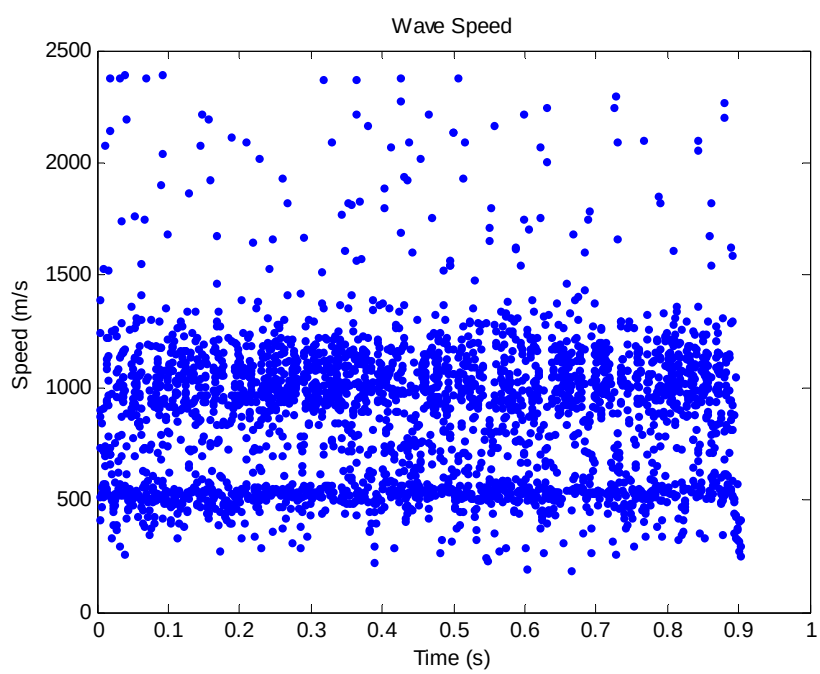

Figure 49. Wave speed data sample 4 φ=1.18, $\dot{m}_{tot}$=24.4 lbm/min, $\dot{m}_f$=0.8 lbm/min

Figures 46-48 are representative of enriched air runs. In the Figs. 46 and 47, the double velocity bands are clearly evident. In Fig. 48 it appears there are three velocity bands, two in the detonation region and one in the non-detonation region. This triple band appears in runs with higher equivalence ratios, total mass flow rates, fuel mass flow rates, and detonation velocities.

Figure 49 is representative of standard air runs. The space between the two bands is not as well defined and there are typically more points above the detonation band than are seen in enriched air runs. This is most likely due to extra noise in the signal.

Again, it is not currently known why the flow reverses direction and further study on this phenomenon is planned. From the current data, it appears that the wave propagates with equivalent speed regardless of the direction in which it is traveling.

APPENDIX D. WAVE FRONT DIRECTION CHANGE

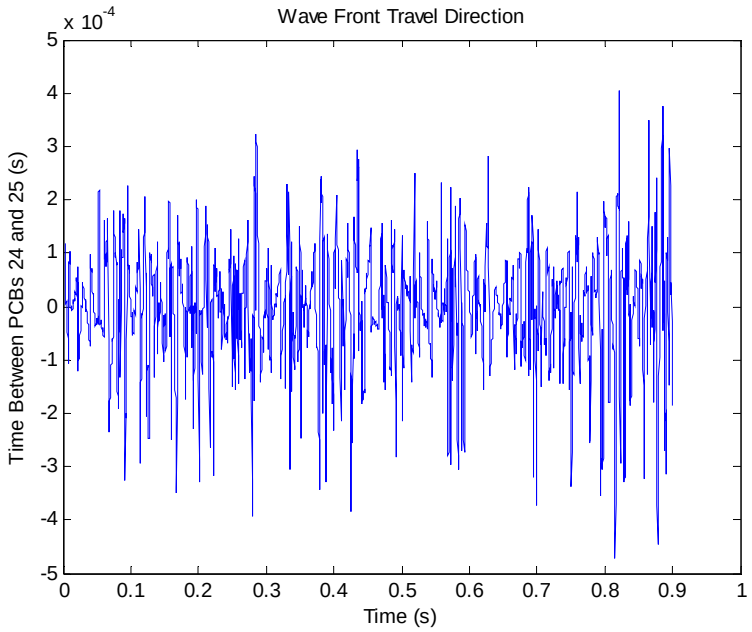

Figure 50. Wave front direction change, enriched air, total mass flow rate of 51.7 lbm/min

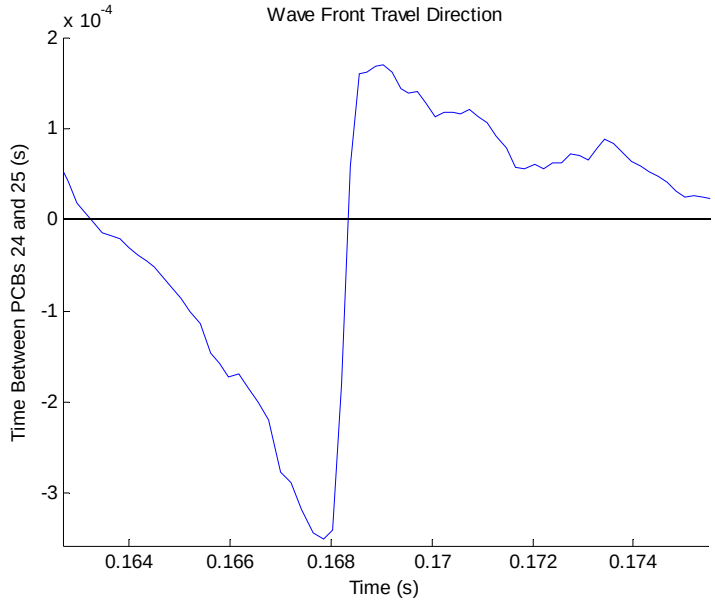

Figure 51. Close up view of Fig. 50

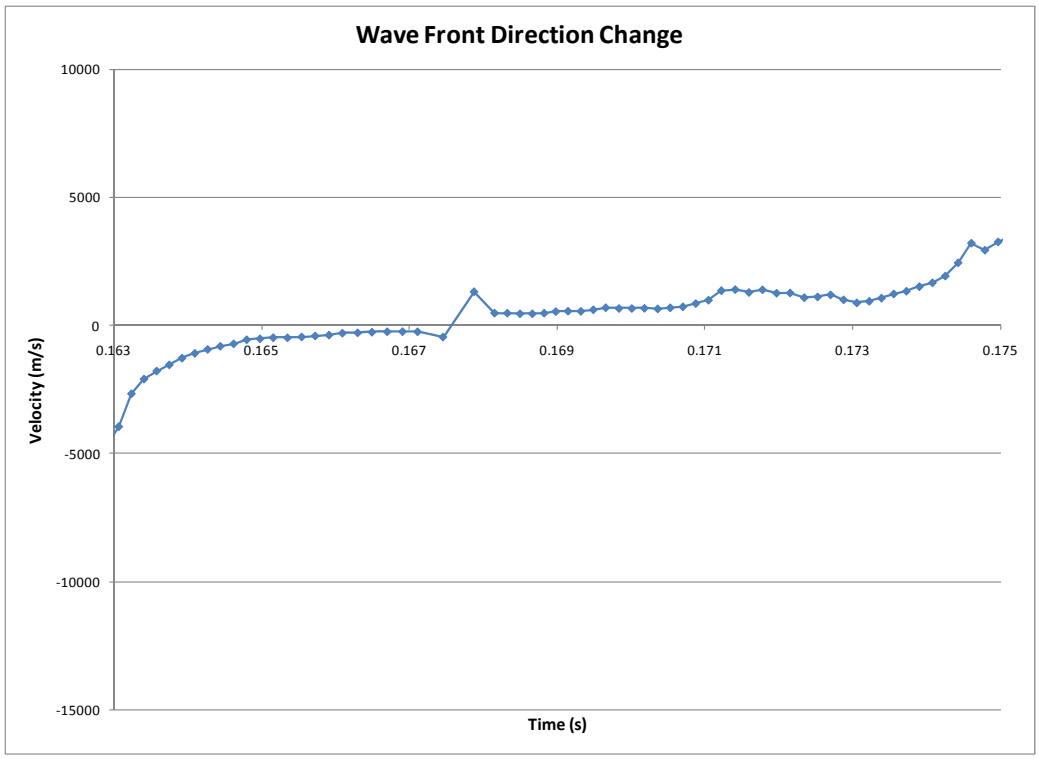

Figure 52. Wave front flow reversal, velocity graph, enriched air, total mass flow rate of 51.7 lbm/min

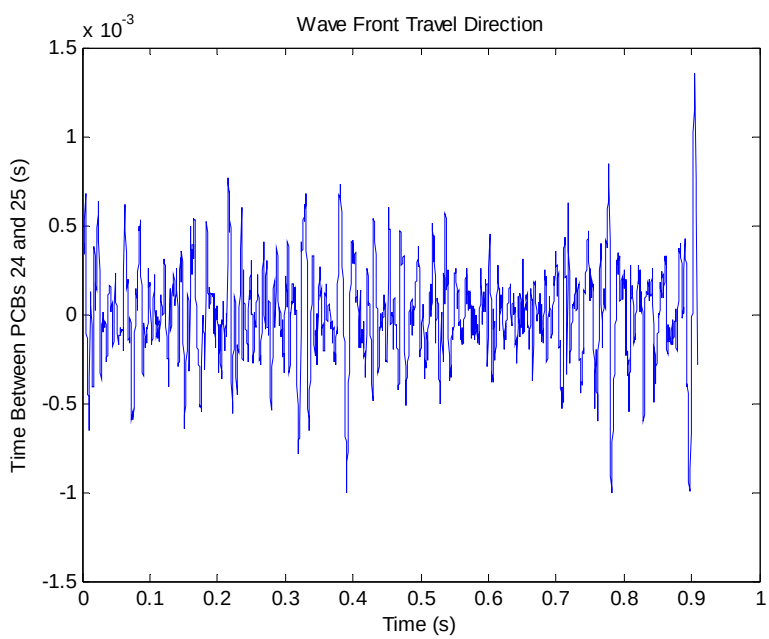

Figure 53. Wave front direction change for standard air, non-repeatable run, total mass flow rate of 23.8 lbm/min

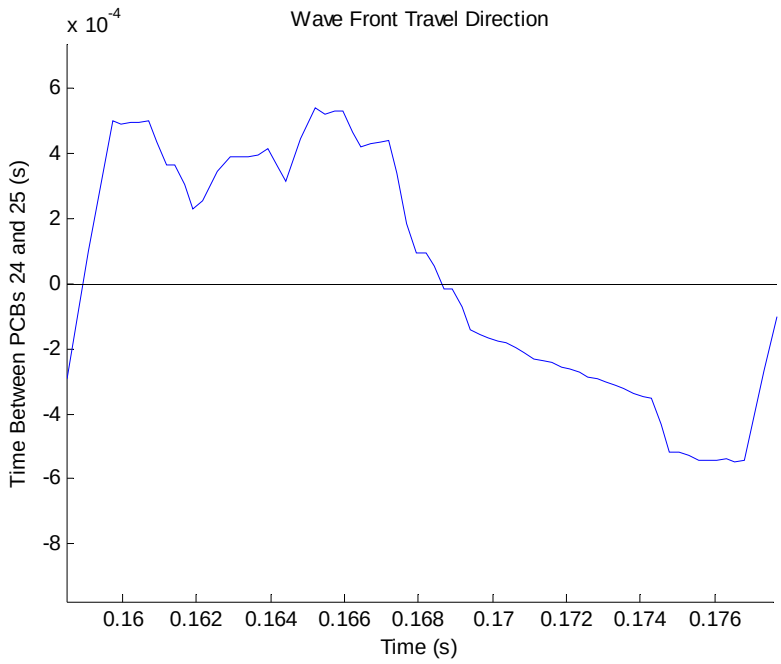

Figure 54. Close up view of Fig. 53

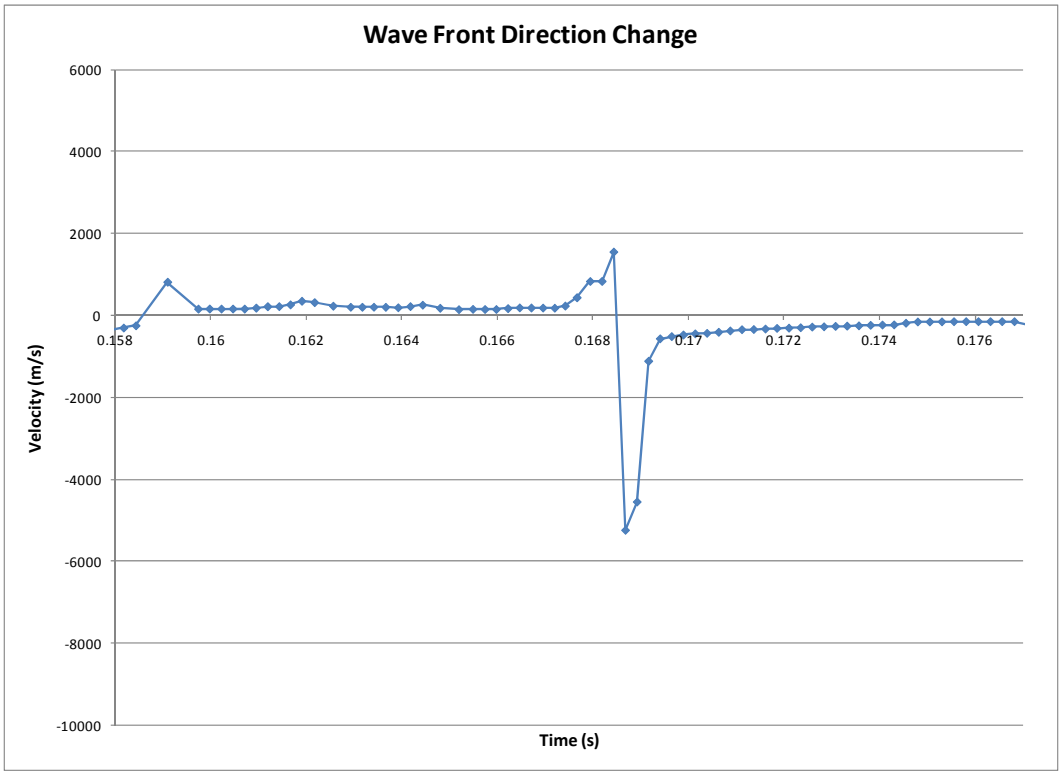

Figure 55. Wave front flow reversal, velocity graph, standard air, non-repeatable run, total mass flow rate of 23.8 lbm/min

APPENDIX E. UNCERTAINTY TABLES

Table E 1. Equivalence Ratio, Total Mass Flow Rate, and Detonation Velocity Errors for Repeatable Enriched Air Runs

φ	φ Error (%)	Total Mass Flow Rate (lb/min)	Total Mass Flow Rate Error (%)	Detonation Velocity (m/s)	Detonation Velocity Error (%)
0.85	0.149	52.3	2.34	1207	25.0
0.86	0.150	51.2	2.34	1213	23.3
0.87	0.154	50.4	2.38	1210	24.2
0.90	0.153	50.4	2.37	1225	24.2
0.92	0.152	50.5	2.36	1240	23.6
0.92	0.150	48.2	2.37	1209	26.6
0.98	0.150	50.6	2.36	1280	21.0
0.99	0.154	45.6	2.39	1231	25.4
0.99	0.153	45.6	2.38	1234	25.1
1.04	0.149	50.7	2.36	1315	20.0
1.05	0.152	42.4	2.41	1219	26.9
1.08	0.151	45.6	2.38	1289	24.2
1.08	0.150	45.5	2.38	1297	24.2
1.08	0.148	50.7	2.35	1337	20.2
1.11	0.149	48.4	2.36	1337	22.5
1.11	0.144	52.7	2.33	1362	19.3
1.11	0.145	53.0	2.35	1359	20.0
1.11	0.145	53.0	2.35	1345	21.1
1.12	0.156	40.2	2.43	1224	29.1
1.13	0.151	45.4	2.40	1309	24.6
1.13	0.151	45.3	2.41	1308	25.3
1.13	0.145	51.7	2.32	1355	20.6
1.13	0.145	51.7	2.33	1355	20.6
1.13	0.144	51.7	2.33	1345	20.6
1.15	0.145	51.4	2.32	1352	21.0
1.16	0.155	38.7	2.43	1224	30.3
1.17	0.147	50.9	2.35	1368	21.5
1.19	0.158	37.5	2.73	1231	34.0
1.19	0.158	37.6	2.73	1232	33.0
1.19	0.154	40.4	2.42	1266	29.7
1.19	0.153	40.3	2.42	1252	28.9
1.24	0.148	46.4	2.36	1371	23.8
1.25	0.148	46.3	2.37	1365	24.1
1.26	0.146	51.0	2.34	1384	21.8
1.26	0.146	51.0	2.34	1401	19.7
1.27	0.152	40.6	2.41	1290	29.9
1.27	0.152	40.7	2.42	1293	29.9
1.33	0.151	40.7	2.41	1308	28.5
1.33	0.150	40.7	2.40	1312	29.7
1.34	0.150	40.5	2.41	1344	26.4
1.34	0.145	51.1	2.34	1418	19.0
1.34	0.145	51.1	2.35	1420	18.7

Table E 2. Air and Fuel Mass Flow Rate Errors for Repeatable Enriched Air Runs

φ	Total Mass Flow Rate (lb/min)	Air Mass Flow Rate (lb/min)	Air Mass Flow Rate Error (%)	Fuel Mass Flow Rate (lb/min)	Fuel Mass Flow Rate Error (%)
0.85	52.3	50.9	2.40	1.4	4.01
0.86	51.2	49.8	2.40	1.4	4.06
0.87	50.4	49.0	2.44	1.4	4.16
0.90	50.4	49.0	2.44	1.4	4.11
0.92	50.5	49.0	2.43	1.4	4.09
0.92	48.2	46.8	2.44	1.4	4.03
0.98	50.6	49.0	2.43	1.5	4.04
0.99	45.6	44.2	2.46	1.4	4.14
0.99	45.6	44.2	2.45	1.4	4.13
1.04	50.7	49.0	2.43	1.6	4.00
1.05	42.4	41.0	2.49	1.4	4.05
1.08	45.6	44.1	2.46	1.5	4.04
1.08	45.5	44.2	2.46	1.5	4.02
1.08	50.7	49.0	2.43	1.7	3.97
1.11	48.4	46.7	2.44	1.7	3.99
1.11	52.7	50.8	2.40	1.8	3.84
1.11	53.0	51.2	2.43	1.8	3.84
1.11	53.0	51.2	2.43	1.8	3.84
1.12	40.2	38.8	2.51	1.4	4.19
1.13	45.4	43.8	2.48	1.6	4.01
1.13	45.3	43.7	2.50	1.6	4.03
1.13	51.7	50.0	2.40	1.8	3.84
1.13	51.7	50.1	2.41	1.8	3.84
1.13	51.7	50.1	2.40	1.8	3.83
1.15	51.4	49.7	2.41	1.8	3.86
1.16	38.7	37.3	2.52	1.4	4.16
1.17	50.9	49.0	2.44	1.8	3.91
1.19	37.5	36.2	2.83	1.4	4.05
1.19	37.6	36.2	2.83	1.4	4.05
1.19	40.4	38.9	2.51	1.5	4.12
1.19	40.3	38.9	2.51	1.5	4.10
1.24	46.4	44.6	2.44	1.8	3.95
1.25	46.3	44.5	2.46	1.8	3.94
1.26	51.0	49.0	2.43	2.0	3.87
1.26	51.0	49.0	2.42	2.0	3.88
1.27	40.6	39.0	2.50	1.6	4.04
1.27	40.7	39.1	2.51	1.6	4.03
1.33	40.7	39.1	2.50	1.7	4.00
1.33	40.7	39.1	2.50	1.7	3.97
1.34	40.5	38.8	2.51	1.7	3.97
1.34	51.1	49.0	2.44	2.1	3.83
1.34	51.1	49.0	2.44	2.1	3.83

Table E 3. Detonation and Non-Detonation Velocity Comparison for Repeatable Enriched Air Runs

φ	Total Mass Flow Rate (lb/min)	Detonation Velocity (m/s)	Non-Detonation Velocity (m/s)	Velocity Ratio	Average Velocity (m/s)
0.85	52.29	1207	577	0.48	1146
0.86	51.18	1213	586	0.48	1174
0.87	50.39	1210	553	0.46	1160
0.90	50.45	1225	575	0.47	1187
0.92	50.47	1240	554	0.45	1203
0.92	48.18	1209	584	0.48	1172
0.98	50.57	1280	554	0.43	1225
0.99	45.63	1231	573	0.47	1160
0.99	45.63	1234	572	0.46	1164
1.04	50.66	1315	522	0.40	1243
1.05	42.40	1219	565	0.46	1130
1.08	45.61	1289	582	0.45	1227
1.08	45.54	1297	581	0.45	1238
1.08	50.73	1337	540	0.40	1293
1.11	48.39	1337	601	0.45	1267
1.11	52.65	1362	614	0.45	1336
1.11	53.02	1359	599	0.44	1339
1.11	53.01	1345	589	0.44	1326
1.12	40.18	1224	571	0.47	1125
1.13	45.39	1309	591	0.45	1252
1.13	45.32	1308	589	0.45	1243
1.13	51.66	1355	589	0.43	1339
1.13	51.72	1355	604	0.45	1336
1.13	51.71	1345	583	0.43	1292
1.15	51.39	1352	620	0.46	1319
1.16	38.72	1224	570	0.47	1114
1.17	50.87	1368	569	0.42	1326
1.19	37.52	1231	585	0.48	1167
1.19	37.60	1232	579	0.47	1155
1.19	40.41	1266	576	0.46	1181
1.19	40.34	1252	568	0.45	1152
1.24	46.42	1371	621	0.45	1315
1.25	46.28	1365	611	0.45	1294
1.26	51.00	1384	594	0.43	1344
1.26	51.00	1401	595	0.42	1374
1.27	40.59	1290	587	0.45	1212
1.27	40.66	1293	584	0.45	1218
1.33	40.73	1308	589	0.45	1229
1.33	40.73	1312	595	0.45	1238
1.34	40.45	1344	609	0.45	1244
1.34	51.13	1418	875	0.62	1396
1.34	51.13	1420	620	0.44	1399

Table E 4. Equivalence Ratio, Total Mass Flow Rate, and Detonation Velocity Errors for Non-Repeatable Enriched Air Runs

φ	φ Error (%)	Total Mass Flow Rate (lb/min)	Total Mass Flow Rate Error (%)	Detonation Velocity (m/s)	Detonation Velocity Error (%)
0.89	0.156	45.8	2.39	1190	25.8
1.20	0.149	44.9	2.38	1335	24.9
1.31	0.158	34.1	2.75	1239	35.5
1.38	0.148	40.9	2.40	1332	27.0
1.42	0.144	51.3	2.32	1441	18.7
1.46	0.147	41.0	2.41	1352	25.3
1.52	0.148	41.0	2.49	1369	24.4
1.59	0.161	24.7	2.66	1197	35.6
1.60	0.171	41.1	3.57	1389	23.1

Table E 5. Air and Fuel Mass Flow Rate Errors for Non-Repeatable Enriched Air Runs

φ	Total Mass Flow Rate (lb/min)	Air Mass Flow Rate (lb/min)	Air Mass Flow Rate Error (%)	Fuel Mass Flow Rate (lb/min)	Fuel Mass Flow Rate Error (%)
0.89	45.8	44.5	2.45	1.3	4.24
1.20	44.9	43.3	2.47	1.7	3.98
1.31	34.1	32.7	2.86	1.4	4.03
1.38	40.9	39.1	2.50	1.7	3.89
1.42	51.3	49.1	2.42	2.2	3.81
1.46	41.0	39.1	2.51	1.8	3.86
1.52	41.0	39.1	2.61	1.9	3.84
1.59	24.7	23.5	2.79	1.2	4.20
1.60	41.1	39.1	3.75	2.0	3.82

Table E 6. Detonation and Non-Detonation Velocity Comparison for Non-Repeatable Enriched Air Runs

φ	Total Mass Flow Rate (lb/min)	Detonation Velocity (m/s)	Non-Detonation Velocity (m/s)	Velocity Ratio	Average Velocity (m/s)
0.89	45.8	1190	569	0.48	1121
1.20	44.9	1335	606	0.45	1255
1.31	34.1	1239	567	0.46	1128
1.38	40.9	1332	603	0.45	1253
1.42	51.3	1441	669	0.46	1407
1.46	41.0	1352	613	0.45	1284
1.52	41.0	1369	628	0.46	1312
1.59	24.7	1197	544	0.45	1046
1.60	41.1	1389	632	0.46	1356

Table E 7. Equivalence Ratio, Total Mass Flow Rate, and Detonation Velocity Errors for 2mm Channel Standard Air Runs

φ	φ Error (%)	Total Mass Flow Rate (lb/min)	Total Mass Flow Rate Error (%)	Detonation Velocity (m/s)	Detonation Velocity Error (%)
0.92	0.208	21.7	2.73	1138	31.1
1.03	0.206	23.5	2.69	1187	28.6
1.15	0.207	21.2	2.73	1133	28.9
1.23	0.157	23.8	2.68	1210	28.6
1.32	0.149	26.8	2.63	1306	28.4
1.46	0.209	16.8	2.85	1034	21.3
1.63	0.210	15.2	2.92	1019	18.3

Table E 8. Air and Fuel Mass Flow Rate Errors for 2mm Channel Standard Air Runs

φ	Total Mass Flow Rate (lb/min)	Air Mass Flow Rate (lb/min)	Air Mass Flow Rate Error (%)	Fuel Mass Flow Rate (lb/min)	Fuel Mass Flow Rate Error (%)
0.92	21.7	21.1	2.80	0.6	6.56
1.03	23.5	22.8	2.77	0.7	6.53
1.15	21.2	20.5	2.81	0.7	6.53
1.23	23.8	23.0	2.77	0.8	4.62
1.32	26.8	25.8	2.73	1.0	4.32
1.46	16.8	16.1	2.96	0.7	6.53
1.63	15.2	14.5	3.04	0.7	6.53

Table E 9. Detonation and Non-Detonation Velocity Comparison for 2mm Channel Standard Air Runs

φ	Total Mass Flow Rate (lb/min)	Detonation Velocity (m/s)	Non-Detonation Velocity (m/s)	Velocity Ratio	Average Velocity (m/s)
0.92	21.7	1138	467	0.41	893
1.03	23.5	1187	430	0.36	821
1.15	21.2	1133	433	0.38	851
1.23	23.8	1210	432	0.36	848
1.32	26.8	1306	382	0.29	724
1.46	16.8	1034	407	0.39	826
1.63	15.2	1019	384	0.38	804

Table E 10. Equivalence Ratio, Total Mass Flow Rate, and Detonation Velocity Errors for 6mm Channel Standard Air Runs

φ	φ Error (%)	Total Mass Flow Rate (lb/min)	Total Mass Flow Rate Error (%)	Detonation Velocity (m/s)	Detonation Velocity Error (%)
1.18	0.145	30.5	2.53	1058	55.0
1.2	0.143	32.1	2.50	1045	48.4
1.22	0.140	35.0	2.46	1067	43.6
1.27	0.141	32.7	2.48	1061	44.2
1.32	0.143	30.0	2.56	1039	47.8
1.32	0.143	30.0	2.53	1038	46.7
1.32	0.143	30.0	2.54	1049	48.5

Table E 11. Air and Fuel Mass Flow Rate Errors for 6mm Channel Standard Air Runs

φ	Total Mass Flow Rate (lb/min)	Air Mass Flow Rate (lb/min)	Air Mass Flow Rate Error (%)	Fuel Mass Flow Rate (lb/min)	Fuel Mass Flow Rate Error (%)
1.18	30.5	29.5	2.62	1.0	4.25
1.2	32.1	31.0	2.59	1.1	4.18
1.22	35.0	33.8	2.54	1.2	4.08
1.27	32.7	31.6	2.57	1.2	4.11
1.32	30.0	28.9	2.65	1.1	4.15
1.32	30.0	28.9	2.63	1.1	4.14
1.32	30.0	28.9	2.63	1.1	4.14

Table E 12. Detonation and Non-Detonation Velocity Comparison for 6mm Channel Standard Air Runs

φ	Total Mass Flow Rate (lb/min)	Detonation Velocity (m/s)	Non-Detonation Velocity (m/s)	Velocity Ratio	Average Velocity (m/s)
1.18	30.5	1058	479	0.45	796
1.2	32.1	1045	491	0.47	818
1.22	35.0	1067	523	0.49	886
1.27	32.7	1061	520	0.49	872
1.32	30.0	1039	497	0.48	820
1.32	30.0	1038	490	0.47	817
1.32	30.0	1049	505	0.48	839

Table E 13. Equivalence Ratio, Total Mass Flow Rate, and Detonation Velocity Errors for 10mm Channel Standard Air Runs

φ	φ Error (%)	Total Mass Flow Rate (lb/min)	Total Mass Flow Rate Error (%)	Detonation Velocity (m/s)	Detonation Velocity Error (%)
0.86	0.140	46.5	2.37	1242	58.4
0.97	0.190	23.2	2.72	1029	68.1
1.00	0.137	52.0	2.35	1250	60.9
1.05	0.146	35.8	2.45	1388	65.9
1.06	0.152	31.2	2.52	1493	65.2
1.07	0.143	39.4	2.41	1322	64.0
1.12	0.160	28.9	2.62	1193	58.1
1.12	0.145	34.5	2.59	1225	56.3
1.16	0.161	27.9	2.65	1193	57.4
1.16	0.146	32.5	2.49	1486	63.3
1.17	0.153	28.7	2.82	1216	60.5
1.17	0.150	28.7	2.63	1214	60.0
1.17	0.149	28.7	2.63	1211	58.7
1.18	0.161	24.4	2.68	1193	59.2
1.20	0.163	24.2	2.72	1189	59.4
1.20	0.150	27.8	2.65	1219	60.7
1.24	0.156	29.2	2.62	1202	59.2
1.30	0.156	27.8	2.64	1210	61.1
1.37	0.164	23.5	2.68	1203	46.0
1.38	0.162	23.4	2.69	1211	44.7
1.44	0.161	23.5	2.68	1207	36.7
1.56	0.156	23.6	2.67	1220	35.6
1.69	0.152	23.7	2.66	1249	32.6
1.83	0.150	23.8	2.66	1257	32.3

Table E14. Air and Fuel Mass Flow Rate Errors for 10mm Channel Standard Air Runs

φ	Total Mass Flow Rate (lb/min)	Air Mass Flow Rate (lb/min)	Air Mass Flow Rate Error (%)	Fuel Mass Flow Rate (lb/min)	Fuel Mass Flow Rate Error (%)
0.86	46.5	45.3	2.43	1.1	4.15
0.97	23.2	22.6	2.79	0.6	5.89
1.00	52.0	50.6	2.41	1.5	4.03
1.05	35.8	34.7	2.52	1.1	4.34
1.06	31.2	30.2	2.59	0.9	4.52
1.07	39.4	38.2	2.48	1.2	4.25
1.12	28.9	28.0	2.70	0.9	4.77
1.12	34.5	33.5	2.67	1.1	4.19
1.16	27.9	26.9	2.73	0.9	4.79
1.16	32.5	31.4	2.57	1.1	4.33
1.17	28.7	27.7	2.92	0.9	4.38
1.17	28.7	27.7	2.71	0.9	4.37
1.17	28.7	27.7	2.71	0.9	4.36
1.18	24.4	23.6	2.77	0.8	4.77
1.20	24.2	23.4	2.82	0.8	4.83
1.20	27.8	26.9	2.74	0.9	4.37
1.24	29.2	28.2	2.71	1.0	4.61
1.30	27.8	26.8	2.73	1.0	4.60
1.37	23.5	22.6	2.78	0.9	4.89
1.38	23.4	22.5	2.79	0.9	4.80
1.44	23.5	22.6	2.79	0.9	4.79
1.56	23.6	22.6	2.79	1.0	4.58
1.69	23.7	22.6	2.79	1.1	4.43
1.83	23.8	22.6	2.79	1.2	4.33

Table E 15. Detonation and Non-Detonation Velocity Comparison for 10mm Channel Standard Air Runs

φ	Total Mass Flow Rate (lb/min)	Detonation Velocity (m/s)	Non-Detonation Velocity (m/s)	Velocity Ratio	Average Velocity (m/s)
0.86	46.5	1242	613	0.49	1050
0.97	23.2	1029	577	0.56	991
1.00	52.0	1250	632	0.51	1014
1.05	35.8	1388	562	0.41	911
1.06	31.2	1493	545	0.37	848
1.07	39.4	1322	575	0.44	945
1.12	28.9	1193	564	0.47	984
1.12	34.5	1225	591	0.48	1077
1.16	27.9	1193	573	0.48	993
1.16	32.5	1486	534	0.36	873
1.17	28.7	1216	584	0.48	1053
1.17	28.7	1214	600	0.49	1057
1.17	28.7	1211	598	0.49	1051
1.18	24.4	1193	590	0.50	990
1.20	24.2	1189	582	0.49	984
1.20	27.8	1219	598	0.49	1057
1.24	29.2	1202	573	0.48	993
1.30	27.8	1210	572	0.47	1000
1.37	23.5	1203	616	0.51	1183
1.38	23.4	1211	637	0.53	1191
1.44	23.5	1207	583	0.48	1180
1.56	23.6	1220	585	0.48	1184
1.69	23.7	1249	584	0.47	1217
1.83	23.8	1257	626	0.50	1230

APPENDIX F. FULL TEST SPACE

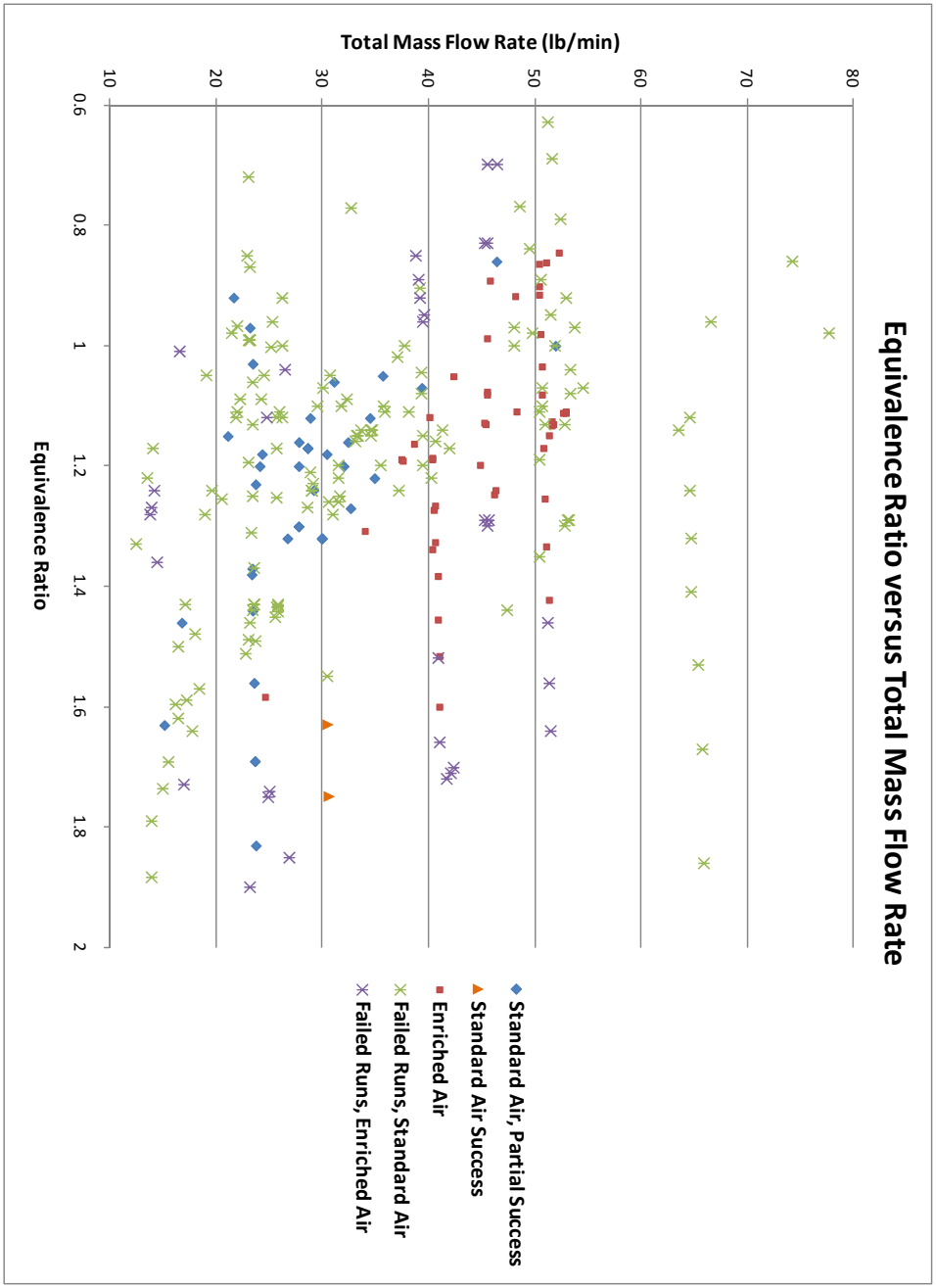

Figure 56. Full test space

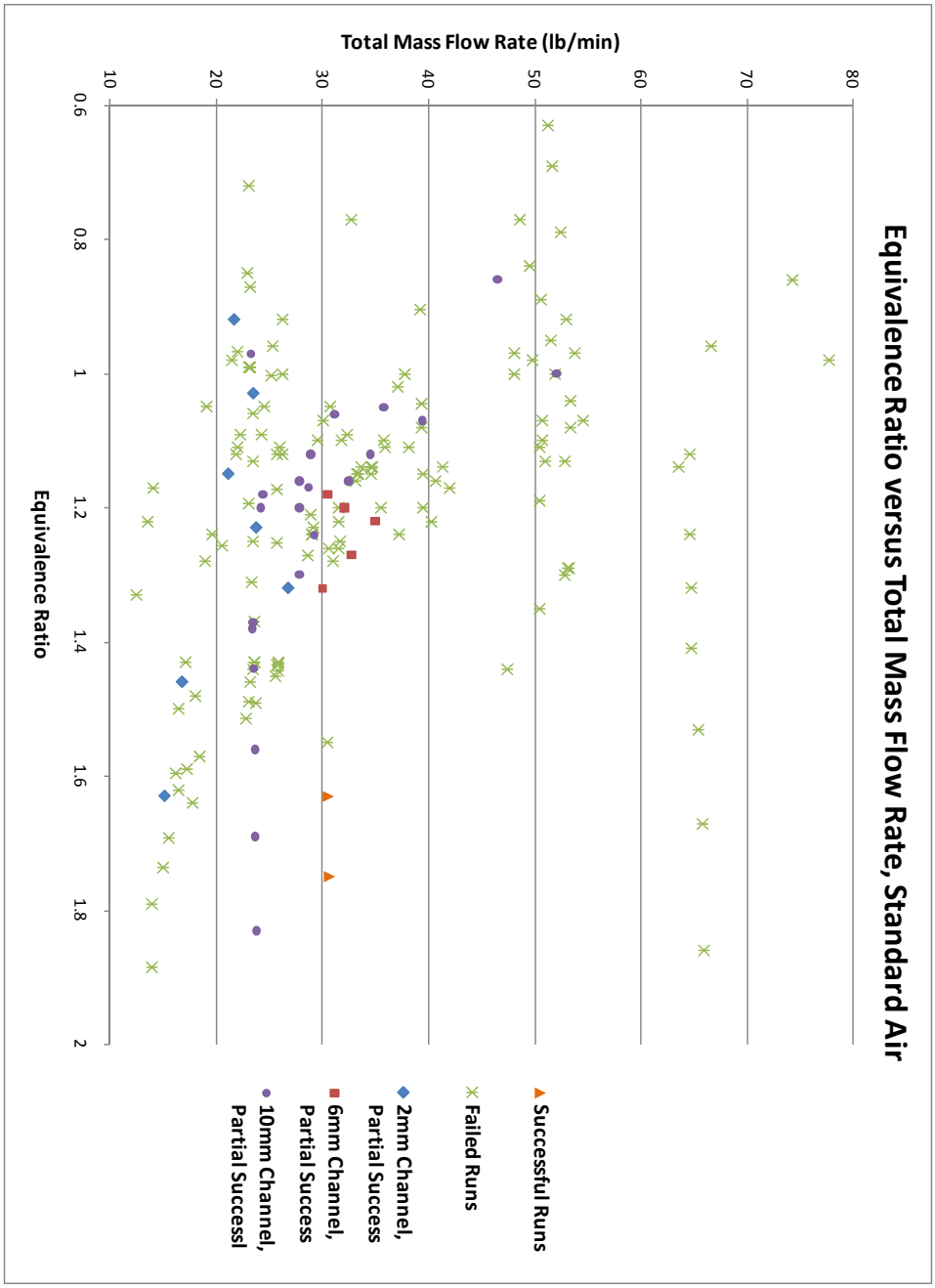

Figure 57. Standard air full test space, partially successful runs delineated by channel width

Figure 56 contains all tests conducted for both standard and enriched air. Failed runs are shown by stars (green for standard, purple for enriched), enriched air runs are designated by red squares, partially successful standard air runs (those which stayed in the channel for 0.9 sec but were not repeatable) are designated by blue diamonds, and the two successful standard air runs are shown as gold triangles. Figure 56 shows that the successful standard air runs were located in a region in which no testing was originally done.

Figure 57 shows the full test space for standard air only. Failed runs are shown by stars, successful runs by gold diamonds, 2 mm channel width partially successful runs by blue diamonds, 6 mm channel partially successful runs by red squares, and 10 mm channel partially successful runs by purple circles. Figure 57 shows that partially successful runs were conducted with all three channels.

Inclusion of partially successful runs in Figs. 56 and 57 serve to illustrate that the operational space could be expanded if the problems with the propellant injection scheme can be mitigated.

REFERENCES

1. Bussing, T. and G. Pappas. "An Introduction to Pulse Detonation Engines," *32nd Aerospace Sciences Meeting and Exhibit*. Reno, NV, January 1994. AIAA 94-0263.

2. Voitsekhovskii, B. V., V. V. Mitrofanov, and M. E. Topchian. "Investigation of the Structure of Detonation Waves in Gases," *Symposium (International) on Combustion*, 12: 829-837 (1969).

3. Bykovskii, Fedor A., Sergey A. Zhdan, and Evgenii F. Vedernikov. "Continuous Spin Detonations," *Journal of Propulsion and Power*, 22: 1204-1216 (2006).

4. Schwer, Douglas A. and K. Kailasanath. "Numerical Investigation of Rotating Detonation Engines," *46th Joint Propulsion Conference and Exhibit.* Nashville, TN, 2010. AIAA 2010-6880.

5. Turns, Stephen R. *An Introduction to Combustion: Concepts and Applications* (2nd Edition). Boston: McGraw-Hill, 2000.

6. Hayashi, Koichi A., et al. "Sensitivity Analysis of Rotating Detonation Engine with a Detailed Reaction Model," *47th AIAA Aerospace Sciences Meeting Including the New Horizons Forum and Aerospace Exposition*. Orlando, 2009. AIAA 2009-0633.

7. Yi, Tae-Hyeong, et al. "A Three-Dimensional Numerical Study of Rotational Detonation in an Annular Chamber," *47th Annual AIAA Aerospace Sciences Meeting.* Orlando, 2009. AIAA 2009-634.

8. Bykovskii, F. A., S. A. Zhdan, and E. F. Vedernikov. "Continuous Spin Detonation of Hydrogen-Oxygen Mixtures," *Combustion, Explosion, and Shock Waves*, 44: 150-162 (2008).

9. Zhdan, S. A. "Mathematical Model of Continuous Detonation in an Annular Combustor with a Supersonic Flow Velocity," *Combustion, Explosion, and Schock Waves*, 44: 690-697 (2008).

10. Bykovskii, F. A., S. A. Zhdan, and E. F. Vedernikov. "Continuous Spin Detonation of Fuel-Air Mixtures," *Combustion, Explosion, and Shock Waves*, 42: 463-471 (2006).

11. Hishida, Manabu, Toshi Fujiwara, and Piotr Wolanski. "Fundamentals of Rotating Detonations," *Shock Waves*, 19 (2009).

12. Thomas, Levi M., et al. "Buildup and Operation of a Rotating Detonation Engine," *49th AIAA Aerospace Sciences Meeting*. Orlando, 2011. AIAA 2011-602.

13. Stevens, Christpher A. *Fuel Composition and Performance Analysis of Endothermically Heated Fuels for Pulse Detonation Engines*. MS Thesis, AFIT/GAE/ENY/09-M21. Graduate School of Engineering and Management, Air Force Institute of Technology (AU). Wright-Patterson AFB OH, March 2009.

14. Kaneshige, Michael and Joseph E. Shepherd. Detonation Database (29 January 2005). April 12, 2011 http://galcit.caltech.edu/detn_db/html/db_12.html.

15. Wheeler, Anthony J. and Ahmad R. Ganji. *Introduction to Engineering Experimentation.* Upper Saddle River : Pearson Prentice Hall, 2004.

16. Falempin, F. "Continuous Detonation Wave Engine," Neuilly-sur-Seine, France, 2008.

17. Cooper, Paul W. *Engineering Explosives.* New York : Wiley-VCH, 1996.

REPORT DOCUMENTATION PAGE		Form Approved OMB No. 0704–0188

The public reporting burden for this collection of information is estimated to average 1 hour per response, including the time for reviewing instructions, searching existing data sources, gathering and maintaining the data needed, and completing and reviewing the collection of information. Send comments regarding this burden estimate or any other aspect of this collection of information, including suggestions for reducing this burden to Department of Defense, Washington Headquarters Services, Directorate for Information Operations and Reports (0704–0188), 1215 Jefferson Davis Highway, Suite 1204, Arlington, VA 22202–4302. Respondents should be aware that notwithstanding any other provision of law, no person shall be subject to any penalty for failing to comply with a collection of information if it does not display a currently valid OMB control number. PLEASE DO NOT RETURN YOUR FORM TO THE ABOVE ADDRESS.

1. REPORT DATE (DD–MM–YYYY)	2. REPORT TYPE	3. DATES COVERED (*From — To*)
16-06-2011	Master's Thesis	Aug 2009-Jun 2011

4. TITLE AND SUBTITLE	5a. CONTRACT NUMBER
Operational Characteristics of a Rotating Detonation Engine Using Hydrogen and Air	5b. GRANT NUMBER
	5c. PROGRAM ELEMENT NUMBER
6. AUTHOR(S)	5d. PROJECT NUMBER
Russo, Rachel M	5e. TASK NUMBER
	5f. WORK UNIT NUMBER
7. PERFORMING ORGANIZATION NAME(S) AND ADDRESS(ES) Air Force Institute of Technology Graduate School of Engineering and Management (AFIT/ENY) 2950 Hobson Way WPAFB OH 45433-7765	8. PERFORMING ORGANIZATION REPORT NUMBER AFIT/GAE/ENY/11-J03
9. SPONSORING / MONITORING AGENCY NAME(S) AND ADDRESS(ES)	10. SPONSOR/MONITOR'S ACRONYM(S)
Intentionally left blank	11. SPONSOR/MONITOR'S REPORT NUMBER(S)

12. DISTRIBUTION / AVAILABILITY STATEMENT
APPROVED FOR PUBLIC RELEASE; DISTRIBUTION UNLIMITED

13. SUPPLEMENTARY NOTES
This material is declared a work of the U.S. Government and is not subject to copyright protection in the United States.

14. ABSTRACT
Rotating detonation engines (RDE) are pressure gain combustion engines that have the potential for greater efficiency than traditional, constant pressure, deflagration engines. RDEs are smaller and mechanically simpler than pulsed detonation engines. A small diameter (3 in) engine was successfully run on hydrogen and air. Most of the tests were conducted using air with a slightly lower diluents percentage (77% nitrogen as opposed to 79% nitrogen). These tests provided the foundation for determining the operational space (mass flow rate and equivalence ratio) of the rotating detonation engine. From the tests conducted with the lower diluents air, the appropriate run conditions for regular air were determined. For standard air (79% nitrogen) it was found that a larger equivalence ratio (about 1.5) was required to obtain continuous detonations.

15. SUBJECT TERMS
Rotating detonation engine, continuous detonation

16. SECURITY CLASSIFICATION OF:			17. LIMITATION OF ABSTRACT	18. NUMBER OF PAGES	19a. NAME OF RESPONSIBLE PERSON
a. REPORT	b. ABSTRACT	c. THIS PAGE	UU	106	Dr. Paul I King
U	U	U			19b. TELEPHONE NUMBER (Include Area Code) (937)255-3636, ext 4628

Standard Form 298 (Rev. 8–98)
Prescribed by ANSI Std. Z39.18